THE *EINSTEIN* TWO-SIGMA CATALOG: SILVER NEEDLES IN THE X-RAY HAYSTACK

EDWARD C. MORAN[1] AND DAVID J. HELFAND
Department of Astronomy, Columbia University, 538 West 120th Street, New York, NY 10027

ROBERT H. BECKER
Physics Department, University of California, Davis, CA 95616; and Institute of Geophysics and Planetary Physics,
Lawrence Livermore National Laboratory, Livermore, CA 94550

AND

RICHARD L. WHITE
Space Telescope Science Institute, 3700 San Martin Drive, Baltimore, MD 21218
Received 1995 June 22; accepted 1995 October 12

ABSTRACT

To facilitate the study of X-ray sources fainter than those contained in the *Einstein* Medium-Sensitivity Survey (EMSS), we have constructed a new catalog of sources and fluctuations exceeding 2 σ significance in 2520 high-latitude *Einstein* IPCC images. We have employed various tests to validate our source-search algorithm for both high- and low-significance sources, and to identify and remove the small number of spurious sources induced by our detection procedure. Based on the known vignetting and background characteristics of the IPC and the measured X-ray log N–log S relation, we have modeled the number of real sources expected in the catalog in order to evaluate its statistical properties below 4 σ significance. Our modeling suggests that ~13,000 sources in the catalog are real celestial X-ray sources, an increase of ~9100 over the number found in previous analyses of the same IPC images. We find that not only is the reliability of the Two-Sigma Catalog a function of source significance σ, it is a function of off-axis angle on the detector as well. The application of different signal-to-noise thresholds at different off-axis angles thus enables one to tune the reliability of the catalog.

The chief motivation for studying large numbers of faint X-ray sources is to search for possible new components of the cosmic X-ray background. To select out real celestial X-ray sources in the Two-Sigma Catalog, we apply astronomical catalogs at other wavelengths as filters. For example, the cross-correlation of the Two-Sigma Catalog with catalogs from surveys of the radio and infrared sky has yielded large samples of faint X-ray sources that are ~90% reliable. Optical spectroscopy of 77 unidentified faint X-ray sources has turned up several surprises, illustrating the merits of selecting X-ray sources using a variety of methods: high-redshift quasars (one at $z = 4.30$), which are absent in the EMSS, X-ray–luminous ($L_x \approx 10^{43}$ ergs s^{-1}) radio-loud elliptical galaxies with optical spectra devoid of emission lines, and infrared-bright active galactic nuclei whose optical spectra are dominated by starburst galaxy features. Follow-up observations are scheduled to determine whether any of these types of objects represent a previously unrecognized component of the X-ray background.

Subject headings: catalogs — galaxies: active — methods: data analysis — X-rays: galaxies

1. INTRODUCTION

Historically, progress in X-ray astronomy has been regulated by the number of celestial high-energy photons available for study. Advancements in mirror and detector technologies, and the resulting gains in the sensitivity, angular resolution, and spectral resolution of successive generations of X-ray observatories, have led to steady improvements in our understanding of the X-ray sky. For example, the use of focusing optics and position-sensitive detectors on the *Einstein Observatory* resulted in the detection of several thousand discrete X-ray sources, a substantial increase over the number found with all the nonimaging instruments that preceded it. *Einstein* sources were detected with arcminute positional accuracy, making, for the first time, identification of the optical counterparts of X-ray sources an efficient process. As a consequence, the study of *Einstein* sources has largely shaped our current knowledge of discrete X-ray source populations.

The imaging proportional counter (IPC) was the primary instrument used on the *Einstein Observatory*. In the years before the launch of *ROSAT*, the ~4000 deg^2 of IPC images represented a unique resource for X-ray astronomers, providing them with ample incentive to characterize fully the IPC, reexamine important early IPC results, and exploit further the IPC data. Better understanding and calibration of the IPC permitted the construction of the *Einstein* Extended Medium-Sensitivity Survey (EMSS; Gioia et al. 1990; Stocke et al. 1991), which contains nearly 8 times as many sources as the original large-area survey (MSS; Maccacaro et al. 1982; Gioia et al. 1984) and remains the largest complete, unbiased, fully identified sample of X-ray sources ever assembled.

The study of the 1–3.5 keV background (XRB) and discrete source contributions to it has perhaps benefited most from more careful treatments of the IPC data. Several important papers have appeared in the literature in past years, fueling the debate over the origin of the XRB. For instance, the luminosity function for active galactic nuclei (AGNs) in this band, derived from the EMSS by Maccacaro et al. (1991), demonstrated that AGNs (of the types represented in the EMSS) contribute no more than ~40% of

[1] Present address: Institute of Geophysics and Planetary Physics, Lawrence Livermore National Laboratory, Livermore, CA 94550.

the XRB flux. Arcminute-scale fluctuation analyses of deep IPC images (Hamilton & Helfand 1987; Barcons & Fabian 1990) showed that the unresolved component of the XRB must come from a population of sources which has a surface density of greater than 1000 deg^{-2}, further constraining the role of quasars. The development of a flat-fielding technique for the IPC, and the determination of the particle contribution to the IPC background, allowed Wu et al. (1991) to derive the IPC spectrum of the XRB. Using these techniques and employing a new source-search algorithm, Hamilton, Helfand, & Wu (1991; cf. Primini et al. 1991) reexamined the *Einstein* Deep Survey fields of Giacconi et al. (1979) and Griffiths et al. (1983), obtaining more accurate measurements of the extragalactic log $N(>S)$–log S relation and the fraction of the XRB in these fields attributable to resolved sources.

With improved characterization of the IPC has come a steady decrease in the source detection signal-to-noise threshold used by various authors; 5 σ was used in the original MSS and Deep Survey studies, 4 σ in the EMSS, and 3.5 σ in the Deep Survey reanalysis of Hamilton et al. (1991). In principle, this threshold can be driven down further, depending on the intended application of the results and one's ability to determine their statistical reliability. In this paper we describe the generation and properties of a catalog of sources and fluctuations in IPC images exceeding 2 σ. Our aim is to cover more sky at fainter flux levels than the EMSS, to complement that survey. We demonstrate several ways in which such a catalog can be used to yield new information about various classes of X-ray sources. In § 2 we outline our selection criteria for the IPC data examined and the source detection algorithm employed in the construction of the catalog. The statistical properties of the catalog and subsequent adjustments designed to improve its reliability are discussed in § 3. Applications of the catalog are described in § 4. Optical spectroscopy for 77 of the new X-ray source counterparts reveals several fascinating discoveries, including the detection of high-redshift ($z \approx 4$) quasars, which are absent in the EMSS sample.

2. THE IPC TWO-SIGMA CATALOG

In order to interpret properly the contents of an astronomical catalog, the data selection criteria and source detection algorithm used to construct it must be understood in detail. This is particularly true for a catalog which purports to contain sources at the 2 σ level. Therefore, in this section we describe how IPC data were selected for analysis and how the selected images were searched for sources. We also present the results of two tests intended to validate our procedures.

2.1. *Manufacture of the Two-Sigma Catalog*

2.1.1. *Data Selection*

There are nearly 4100 IPC images covering ~ 1 deg^2 each in the *Einstein* database. Exposure times for these fields range from approximately 100–56,000 s, and pointings are located all over the sky. At 2.0 σ, the contents of our catalog will be dominated by spurious detections. We specifically want to exclude, therefore, any data in which the spurious detection rate is likely to be higher than that dictated by statistics alone. Since the X-ray images used in the EMSS were chosen carefully to include only the cleanest data, several of the sound guidelines for selection of the data used

in that survey were adopted here (see Gioia et al. 1990). However, because we do not have the same ambitions for completeness as the EMSS, we have included more (and slightly different) data.

Sources of bright, diffuse emission are the chief breeding ground for large numbers of spurious 2 σ sources independent of the detection algorithm employed. Therefore, we excluded all IPC images centered within 10° of the Galactic plane (eliminating most Galactic supernova remnants) and fields within the boundaries of the Magellanic Clouds (which have regions of intense diffuse emission; Wang et al. 1991). This biases the mix of real celestial sources in the catalog toward extragalactic objects, but allows us to minimize the confusion caused by Galactic stars when we set out to identify their optical counterparts (§ 4). Next, we visually inspected the 2981 images remaining after these exclusions for obvious sources of diffuse emission. On the basis of this inspection, we excluded 187 additional fields containing bright Abell galaxy clusters, regions of diffuse emission in the Virgo Cluster, high-latitude supernova remnants, and regions crowded with Galactic sources, such as the Orion and Pleiades fields. As discussed in § 3.1 below, even slightly extended sources can lead to the detection of several spurious sources. Therefore, we also excluded any image in which a target Abell cluster appears more extended than $\sim 10'$. In addition, several IPC targets were observed multiple times, usually for variability studies. If one image in a series of redundant images had substantially more exposure time (more than about twice as much as any others), we excluded the shorter exposure fields. If, on the other hand, shorter exposure fields had different roll angles and sampled somewhat different parts of the sky, or if no image in a series offered a clear advantage in exposure time, redundant images were kept. Finally, images with less than 300 s of good exposure time were omitted.

The total number of IPC images used to construct our catalog is 2520, as compared to 1435 included in the EMSS. We exclude in each image four 4' strips centered on the window support ribs, but we have not excluded data near the center of the field; thus, our catalog includes the targets of the IPC observations as well as serendipitous sources elsewhere in the field of view. The area of sky examined in each field is 0.75 deg^2, compared to 0.6 deg^2 in the EMSS. Excluding redundant fields, our catalog covers 1850 deg^2, a factor of 2.3 more than the EMSS. The mean and median exposure times for our sample of images are 3900 and 2200 s, respectively. The distribution of image exposure times for the data used to construct our catalog is shown in Figure 1.

2.1.2. *Source-Search Algorithm*

Having selected only data which will not enhance the number of spurious sources in our catalog, we also want to be certain that the detection algorithm we use does not systematically generate spurious sources. Our source-search algorithm is based on the one developed by Hamilton et al. (1991) for their reanalysis of the IPC Deep Survey fields, and several of our steps are identical to theirs. However, when we used their algorithm explicitly to construct a preliminary version of the Two-Sigma Catalog, systematics were found to be present in the catalog below ~ 3.5 σ (discussed further in § 2.2.2). Thus, we were forced to interrogate each step in the source detection procedure, to reduce the spurious source fraction and to improve the accuracy of our detections of real sources. There are no
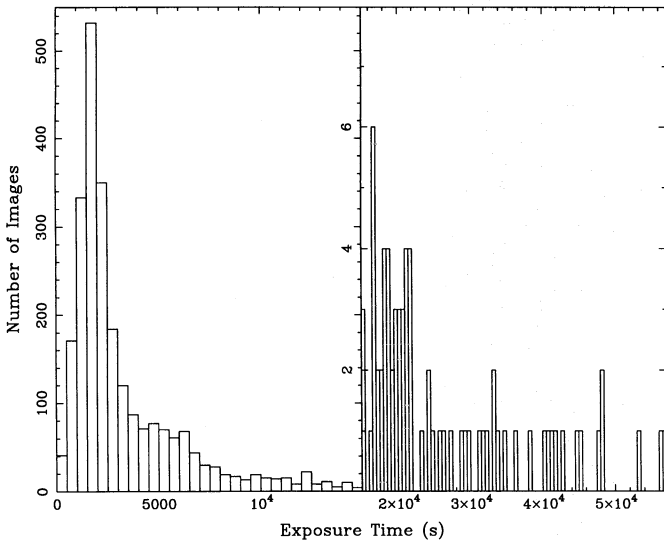
Fig. 1.—Distribution of exposure times for the 2520 IPC images used to construct the Two-Sigma Catalog.

which the signal-to-noise threshold for detection, σ_{th}, is lowered with each successive iteration. We perform five iterations, with $\sigma_{th} = 10, 6, 4, 3,$ and 2. In any iteration, the "most significant" pixel, i.e., the one centered on the source with the highest signal-to-noise ratio σ exceeding σ_{th}, is examined first for a source. Provided that the source meets the sampling requirements—at least $\sim 60\%$ of the source pixels and $\sim 30\%$ of the annulus pixels are unshadowed and undeleted—the source is considered detected. After the source parameters are recorded, the pixel values for the source region are blanked in the count and exposure maps. The radius to which data are deleted is proportional to $\ln \sigma$, an empirically determined value found to be suitable for typical spectrum sources over a wide range of σ (however, see § 3.1 below). The procedure continues to the next most significant source with $\sigma > \sigma_{th}$. If within an iteration the number of undeleted source or annulus pixels for a source decreases as a result of the excision of a brighter nearby source, the detection of this source is deferred to the next iteration. When no more sources with σ above the current threshold are left, the signal-to-noise ratios are recomputed at each of the remaining pixels, excluding the deleted data, and σ_{th} is lowered appropriately for the next search iteration.

The advantages of the use of a flat field and a locally determined background for the detection of faint IPC sources were discussed in detail by Hamilton et al. (1991). We have made several minor modifications to their detection scheme, the most salient of which we summarize here:

1. We search for sources in order of their brightness, not by scanning, as in the sliding-box methods often employed in automatic search procedures. This ensures that the significance of a source is not compromised by the presence of brighter sources in its background annulus and greatly reduces the number of "edge effect" 2σ sources found near the edges of the IPC and along the window support ribs.

2. We iteratively decrease the signal-to-noise threshold for detection, σ_{th}, in several stages, recomputing σ at each undeleted pixel between iterations. Furthermore, we defer detection of sources "corrupted" by the deletion of a nearby brighter source to a subsequent search iteration. Again, these strategies improve the accuracy of our computed source significances.

3. We have increased the size of the background annulus and have made more stringent requirements for the minimum area used to compute the background level. This also reduces the number of spurious detections at the lower values of σ.

In concert, these modifications have improved the accuracy of our detections and have afforded us consistent, predictable behavior regarding the detection of the faintest sources, as we demonstrate in § 2.2.

A total of 49,537 sources are found in 2520 IPC images, using the above procedure. Some sources in redundant images appear in the catalog more than once. In such cases we keep only the entry with the highest signal-to-noise ratio. After removal of duplicate sources and the spurious "satellite sources" identified in § 3.1, 46,186 sources remain. Of these, 4764 have significances greater than 3.5 σ, compared to 3912 sources with significances greater than 3.5 σ in the same 2520 images in the *Einstein* 2E Catalog, assembled by the Smithsonian Astrophysical Observatory (SAO).

substantive philosophical differences between our new procedure and that described by Hamilton et al. (1991); our modifications have merely optimized the algorithm for the detection of sources fainter than those they considered. This has come at the expense of computing efficiency; however, since the entire photon event database is on line at Columbia, the complete search takes as little as 12 hours.

Our procedure begins with the construction of two maps for each satellite orbit (called a HUT): one for the counts and one for the exposure time (which is initially constant across an image and is equal to the "good" exposure time for the HUT). We use data in the pulse-height–invariant (PI) channels 2–10, which covers the energy range 0.16–3.5 keV, collected when the Sun-angle viewing geometries (VG) were most favorable (i.e., VG = 1–3). We have opted to bin the IPC data in $32'' \times 32''$ pixels, rather than pixels 4 times as large, as was done by Wu et al. (1991) and Hamilton et al. (1991). This permits the use of a detection cell which better samples the IPC point response function. The IPC flat field (Wu et al. 1991) is applied to the exposure map for each HUT, accounting for energy-dependent vignetting due to the *Einstein* optics and spatial nonuniformities in the IPC response. Next, the count maps for all HUTs in an observation are combined in sky coordinates, as are the exposure maps.

In the next step, we compute the signal-to-noise ratio at each pixel in the image as though a source were centered there. Potential source counts n_S are collected within $1.'25$ of this central pixel, and background counts are collected from within a concentric annulus with inner and outer radii of $3'$ and $6'$. In practice, this means that there are 21 pixels in the source aperture, covering 5.97 arcmin^2, and 304 pixels in the background annulus, covering 86.5 arcmin^2 (if both source and annulus are unshadowed). The number of background counts n_B expected within the source aperture is the number of counts in the background annulus weighted by the relative areas of the source and annulus and the mean flat-field values in the two regions. The signal-to-noise ratio is computed using the formula $\sigma = n_S/(n_S + n_B)^{1/2}$. This procedure is carried out for every pixel in the IPC image.

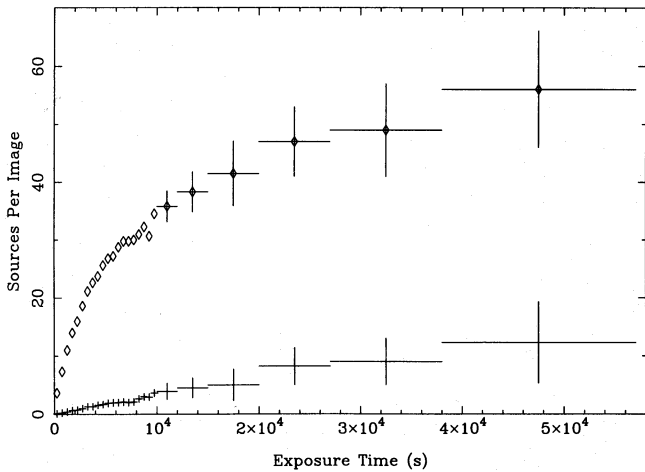The search for sources occurs in an iterative fashion, in

FIG. 2.—Mean number of sources detected per IPC image, as a function of exposure time. The upper set of points (*diamonds*) is for all sources in the Two-Sigma Catalog. The lower set of points (*crosses*) is for the subset of sources with $\sigma > 4$. The larger crosses at exposures above 10^4 s indicate the approximate range in each exposure time interval.

How many of the entries in the Two-Sigma Catalog are celestial X-ray sources? As a first attempt to answer this question, we have plotted in Figure 2 the average number of sources detected per image as a function of exposure time. The number of sources (at all σ) rises steeply from ~ 3 per field at the shortest exposure times, to ~ 25 per field at an exposure time of 5000 s, then increases more slowly to a maximum value of ~ 60 per field. In other words, there is an increase of a factor of 8 over the first decade in exposure time, and a factor of 2 increase over the second. By contrast, the mean number per field of sources with significances greater than 4σ, which should indicate how the relative number of real sources per field depends on exposure time, increases by a factor of ~ 10 over both decades. Spurious sources must be largely responsible for the distribution of the upper sets of points in Figure 2, but the exact nature of their contribution is not clear. In § 3.2 we discuss statistical methods for understanding the spurious source contribution to the catalog.

2.2. *Validation of the Catalog*

The ultimate utility of the Two-Sigma Catalog depends entirely on the effectiveness of the source-search algorithm discussed above. We have performed two tests designed to validate our algorithm for the detection of both high- and low-significance sources.

2.2.1. *Comparison to EMSS Sources*

The EMSS contains 835 serendipitously discovered sources detected above 4σ in 1435 high-latitude IPC images (Gioia et al. 1990). Being the largest single compilation of carefully selected *Einstein* sources assembled to date, the EMSS serves naturally as an important benchmark for extensions of the IPC database such as our catalog. Although the EMSS sources were extracted using procedures very different from ours (see Harnden et al. 1984), a comparison of the signal-to-noise ratios for our detections of EMSS sources with those published in the EMSS itself is an excellent means for examining the behavior of our source detection algorithm for high-significance sources.

Figure 3 displays the results of that comparison. We have

applied our source-detection program to the same 1435 images used to construct the EMSS. Immediately clear from Figure 3 is that all sources fall very close to the identity line with little dispersion about that line. The dispersion appears to increase somewhat at lower values of σ, with 4σ EMSS sources having significances in our catalog between $\sim 3\sigma$ and 6σ. Our versions of the EMSS sources actually tend to have somewhat higher signal-to-noise ratios, but only by an average amount of 0.15σ. Thus, our automatic source-search procedure appears to work as well as, if not better than, detection schemes employed in the past for high-significance IPC sources. However, most of the sources in our catalog are *below* 4σ, and the important test for our source detection algorithm concerns its behavior regarding weaker sources.

2.2.2. *Location of Sources on the IPC*

It is difficult to measure how well a procedure detects real sources below 4σ because so many of the "sources" at that level of significance are, in fact, spurious. A useful diagnostic is provided by the distribution of source positions in the IPC detector coordinate system. While this distribution cannot provide a quantitative means for testing the efficacy of the source detection scheme, it provides a powerful qualitative one. For instance, we would expect the distribution of sources on the IPC to be approximately uniform with an excess at the center of the detector due to targets. In fact, the plot of the source distribution for an early version of our catalog showed strong enhancements and deficits of sources in regions parallel to the charge collection wires in the IPC and in the corners of the field. Furthermore, we found that the pattern changed as parameters such as the size of the background annulus were varied.

Figure 4*a* (Plate 3) shows where sources in our final catalog are found in detector coordinates. The plot contains
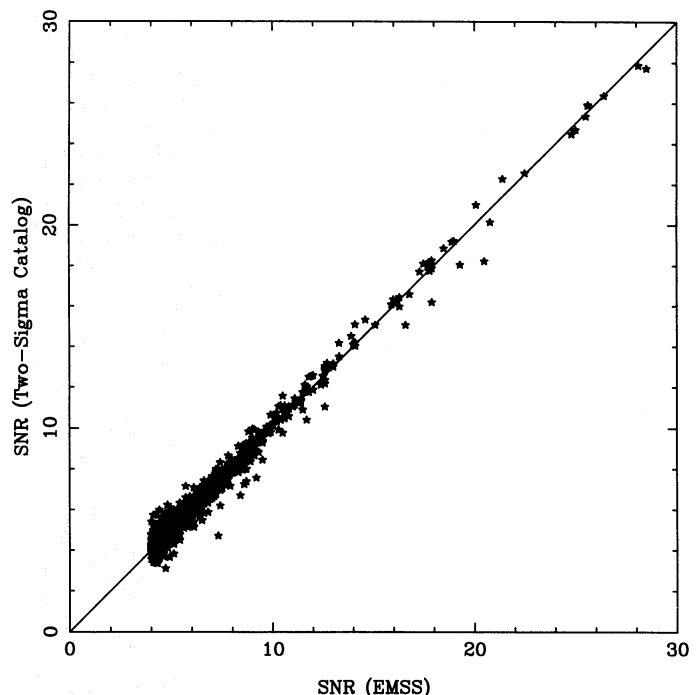

FIG. 3.—Significance of our detections of EMSS sources compared to those published in the EMSS itself. One $\sim 40\sigma$ source, which falls very close to the identity line, is not shown.
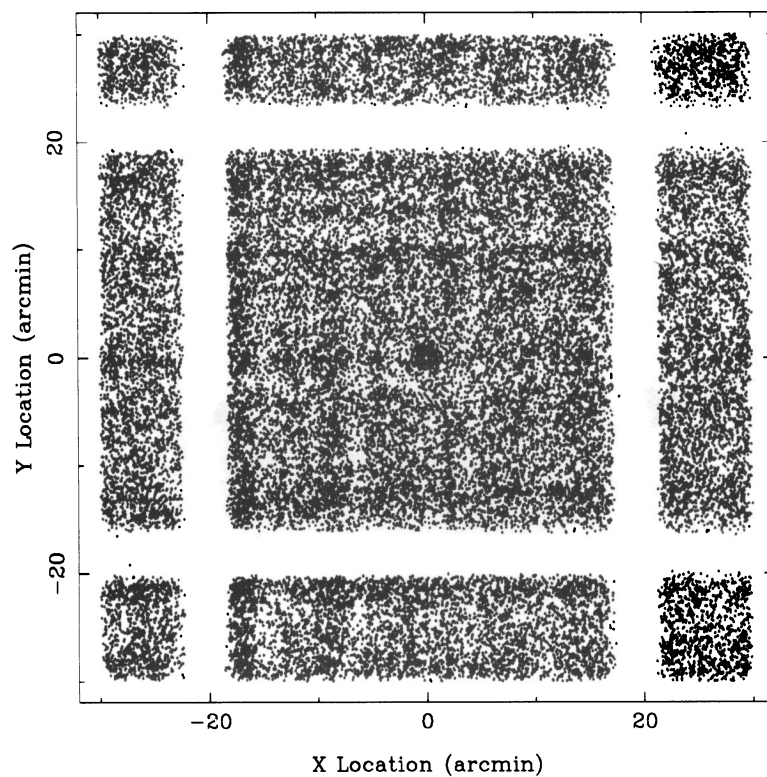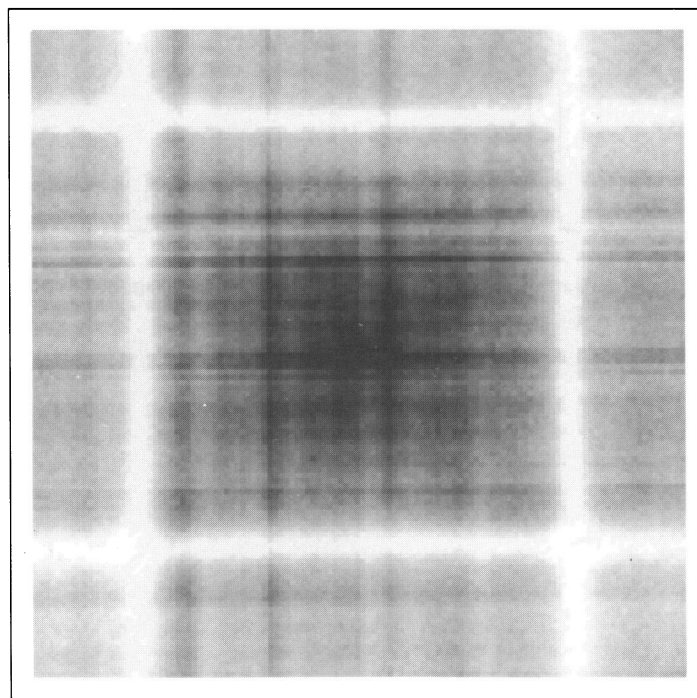
PLATE 3

FIG. 4a

FIG. 4b

FIG. 4.—(a) Location on the IPC of sources in the Two-Sigma Catalog; (b) the IPC flat field. Comparison of (a) and (b) indicates that more/fewer sources were detected in places where the IPC is more/less sensitive. The white bars correspond to the IPC window support ribs.

MORAN et al. (see 461, 130)

only sources detected in IPC images with single roll angles, since sources in fields with multiple roll angles have more than one set of corresponding detector coordinates. Thus, ~39,000 of the ~46,000 sources in the catalog are represented in Figure 4a, and 93% of these are below 4 σ. The excess of sources at the center of the detector due to targets, and the lack of sources where data near the ribs have been deleted, are obvious. Otherwise, it appears that the distribution of sources is roughly uniform. Some faint structure parallel to the charge collection wires remains present in the source distribution. But compare this source distribution to the IPC flat field, displayed in Figure 4b, which also shows structure parallel to the charge collection wires. The pattern of sources on the IPC mimics *in detail* the flat field. Darker regions on the flat-field image represent areas where the detector is more sensitive. Thus, we are finding more sources at places where the detector is more sensitive, exactly what should happen if the excess sources are real.

To test this assertion, we divided the Two-Sigma Catalog into two parts, separating sources detected where the flat-field values are above the median value from those detected where the flat-field values are below the median. Sixty-three percent of the sources are detected where the flat field is above the median value. Next, we cross-correlated each subcatalog with the Green Bank 6 cm radio catalog (this procedure is described in § 4.1.1). Seventy-two percent of the X-ray sources that match 6 cm radio sources are from the "above-the-median" subcatalog, and the fraction of matches expected to arise by chance is significantly less for these (9% vs. 12%). This tells us that the excess sources found where the detector is more sensitive are predominantly real sources. This result is an important confirmation of the flat-fielding procedure and a strong endorsement of our detection algorithm. In the next section we determine exactly what fraction of sources in the catalog, as a function of the signal-to-noise ratio, are real celestial X-ray sources.

3. STATISTICAL PROPERTIES OF THE TWO-SIGMA CATALOG

Having established that our methods for constructing the IPC Two-Sigma Catalog are qualitatively well behaved, quantitative analysis is needed to determine the usefulness of the catalog as well as its limitations. In this section we explore a way of finding and removing spurious sources that are artifacts of our source detection scheme. We then model the number of real X-ray sources expected to be present in the catalog, thereby determining the spurious source detection rate as a function of the signal-to-noise ratio and the location on the detector.

3.1. Removal of "Satellite" Sources

We are confident that searching for sources in order of significance, rather than scanning for them, makes the most sense when a local background is used and when sources are deleted after detection. However, in the implementation of our detection algorithm we have had to assume that all sources we detect are point sources and that they have approximately the same spectrum, neither of which is strictly true. In certain instances, these assumptions lead to insufficient data being deleted after the detection of a source. For bright, extended sources the reasons are obvious; this is why we were careful to exclude images containing extended sources and diffuse emission. But similar

problems can arise for some point sources as well. The point response function (PRF) for the IPC is characterized by two components: (1) a quasi-Gaussian core, the exact shape and width of which are determined by the geometric figure of the optics and the event-centroiding capabilities of the IPC, and (2) non-Gaussian wings, caused by X-rays being scattered to wide angles by mirror microroughness. Both of these components have a strong spectral dependence. For soft X-rays, the core of the PRF is broader than it is for hard X-rays, because soft X-rays deposit less charge on the detector wires, making the determination of event centroids less accurate. Mirror scattering, on the other hand, is much more severe for hard X-rays, and a higher fraction of them are scattered out of the core and into the wings. Thus, especially soft- or hard-spectrum sources (e.g., stars or some AGNs) will tend to have a nonnegligible fraction of counts outside the deletion radius, which has been set for sources with typical spectra. These undeleted counts might then be detected as independent "satellite" sources in a subsequent iteration of our detection procedure.

To test for this effect, we cross-correlated the Two-Sigma Catalog with itself to see whether sources tend to be found close to bright sources above the level expected by chance. For a given "primary" source of significance σ_1, only matches to it with sources having $\sigma < \sigma_1$ in the same image were considered. The accumulated results for the number of matches to primary sources as a function of positional offset are displayed in Figure 5. The primary sources are grouped by σ_1, and the number in each offset bin has been normalized by the solid angle of the annulus represented by the angular range of that bin. The resulting distribution is constant at each offset if the two sets of objects being compared are positionally uncorrelated, making the identification of a correlation straightforward.

Each panel in Figure 5 has qualitatively the same characteristics. The number of matches is zero out to the deletion radius determined by σ_1 and is approximately constant at large position offsets, as expected. However, at offsets just beyond the deletion radius, excesses of sources are observed. These are satellite sources and should be deleted from the catalog. Of course, there are also real celestial X-ray sources at small offsets as well, but the fraction of these determined from the observed source density at a given σ is low (19%–29%). Instead of removing every source within a certain distance of a bright X-ray source, we only remove those below 5 σ, to recover some of the real sources at small offsets. This procedure flags 1729 entries in our catalog, the removal of which leaves 46,186 sources in the final *Einstein* Two-Sigma Catalog. It is interesting that a strong correlation is observed even in the 4–6 σ range for primary sources. We suspect that the satellite sources in these cases are largely due to faint but extended primary sources, rather than point sources with unusually hard or soft spectra, since the magnitude of the number of undeleted counts in the latter case is expected to be small. This could be confirmed by the new search for extended sources in the IPC database being conducted by Oppenheimer, Gaidos, & Helfand (1996).

3.2. The $N(>\sigma)$–σ Relation

With the removal of the satellite sources, the Two-Sigma Catalog is now largely free of sources induced by our detection procedure. But before we use the catalog for astronomical purposes, we would like to gauge its reliability. A

potentially useful diagnostic is the median signal-to-noise ratio σ_m, which can be computed for various ranges of exposure times and/or positions on the IPC. Exposure times for the IPC images included in our study vary by more than 2 orders of magnitude, and in a single image the effective

exposure time varies by roughly a factor of 3 between the center and the edge of the field of view. Luckily, the X-ray log $N(>S)$–log S relation has an approximately constant slope over the range of limiting sensitivities represented in the data (Hasinger et al. 1993). Therefore, σ_m for real X-ray sources in our catalog should be independent of exposure time *and* location on the IPC. In addition, spurious sources—the fraction of which increases as σ decreases—should not show any preference for location on the IPC; their presence will decrease σ_m but should not alter its spatial constancy. However, as displayed in Figure 6, σ_m for sources in our catalog *decreases* with off-axis angle. This must mean that, at a given value of σ, the fraction of spurious sources increases with off-axis angle. Thus, we have an indication that the reliability of the catalog is a function of source location on the detector.

Being optimists, we have decided to model the fraction of real—rather than the spurious—sources in the Two-Sigma Catalog. This begins with the assumption that the soft X-ray log $N(>S)$–log S relation, expressed

$$N(>S) = N_0 S^{-\alpha}, \qquad (1)$$

has a constant slope α, which has been measured to be 1.5 using the EMSS (Gioia et al. 1990) and 1.7 at somewhat lower fluxes using *ROSAT* (Hasinger et al. 1993). We adopt $\alpha = 1.5$ in our calculations below. Next, we assume that the spectra of the X-ray sources are similar and, therefore, that a direct proportionality exists between the count rate for an X-ray source and its energy flux. The counts-to-flux conversion customarily adopted for *Einstein* IPC sources is 1 count s^{-1} = 2.4×10^{-11} ergs cm^{-2} s^{-1}. This corresponds to the assumption of a power-law spectrum with $\Gamma = 2$ and an absorbing column $N_H = 2 \times 10^{20}$ cm^{-2}. From the definition of the signal-to-noise ratio $\sigma = St^{1/2}/(S + B)^{1/2}$, where S and B are the source and background count rates
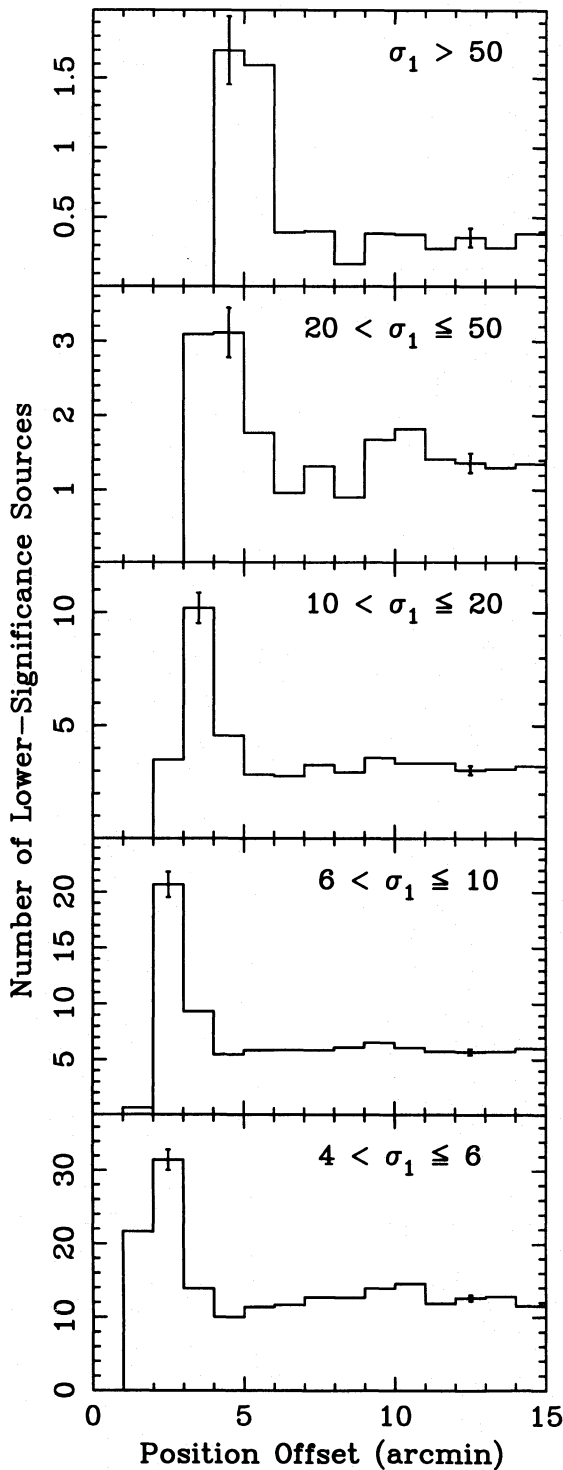

Fig. 5.—Number of lower significance sources in the Two-Sigma Catalog as a function of position offset from higher significance sources in the range indicated by σ_1. The number in each offset bin has been normalized by the solid angle (in arcmin^2) of the annulus that represents the offset range covered by the bin. The peak at small offsets in each panel is due to spurious "satellite sources," which result when not enough data are deleted after the detection of an extended or extreme-spectrum source. The 1 σ error bars indicate that the effect is not statistical.

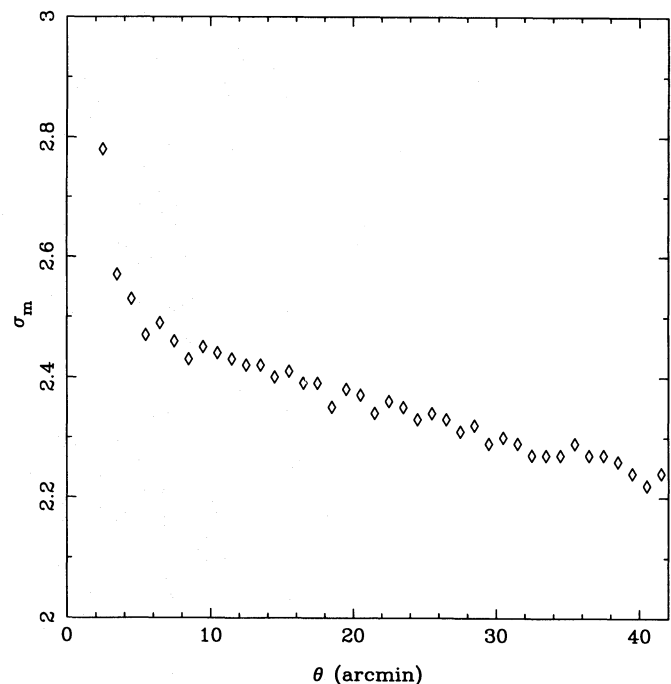Fig. 6.—Median signal-to-noise ratio σ_m of sources in the Two-Sigma Catalog as a function of off-axis angle θ. On-axis, σ_m is determined mainly by targets; σ_m decreases steadily off-axis.

and t is the exposure time, we obtain an expression for S in terms of σ:

$$S = \frac{\sigma^2 + \sqrt{\sigma^4 + 4Bt\sigma^2}}{2t}. \qquad (2)$$

Substituting this in equation (1), the $N(>\sigma)$ relation is derived:

$$N(>\sigma) = N_0 \left(\frac{\sigma^2 + \sqrt{\sigma^4 + 4Bt\sigma^2}}{2t} \right)^{-\alpha}. \qquad (3)$$

Ultimately, we wish to compare directly the number of sources expected in a particular σ interval with the actual number present in the Two-Sigma Catalog; therefore, it is not the integrated number of sources above some σ that we are after, but rather the differential source counts $n(\sigma)$, given by

$$N(>\sigma) = \int_\sigma^\infty n(\sigma')d\sigma'. \qquad (4)$$

Thus, differentiating equation (3) and applying the appropriate limits, we obtain the expression for the differential source counts:

$$\begin{aligned} n(\sigma) &= -\frac{dN(>\sigma)}{d\sigma} \\ &= \alpha N_0(2t)^\alpha [\sigma^2 + (\sigma^4 + 4Bt\sigma^2)^{1/2}]^{-\alpha-1} \\ &\quad \times \left[2\sigma + \frac{1}{2}(\sigma^4 + 4Bt\sigma^2)^{-1/2}(4\sigma^3 + 8Bt\sigma) \right]. \quad (5) \end{aligned}$$

We have used IPC images with a wide range of exposure times; in addition, since vignetting affects some sources of background but not others, the background characteristics vary across the face of the detector. Thus, equation (5) must be modified to accommodate these circumstances. To deal with exposures of different duration, we compute $n(\sigma)$ for exposure times t spaced at 500 s intervals over their entire range, weight the calculations by a normalized distribution function $f(t)$, and sum the results. The function $f(t)$ is derived from the image exposure times displayed in Figure 1. In addition, vignetting due to the *Einstein* optics substantially reduces the effective exposure time at off-axis field angles θ, so exposure times must be modified by the normalized vignetting function $v(\theta)$ (see Wu et al. 1991).

The adjustment for spatial variations in the background is more complicated. Both source counts and background counts from the X-ray background and solar-scattered X-rays are vignetted, but the particle background is not (Wu et al. 1991). Hence, the background rate B consists of two parts: B_X for the vignetted X-ray background, and B_P for the particle background. B_P was determined in two independent ways by Wu et al. (1991), who derived a mean value of $\sim 1.4 \times 10^{-4}$ counts s^{-1} arcmin^{-2}. The total background rates for source-subtracted IPC images are strongly clustered near 1.6 counts s^{-1} (Fig. 7); thus, the mean photon background rate is $\sim 4.5 \times 10^{-4}$ counts s^{-1} arcmin^{-2}. Assigning B_X the appropriate on-axis value of 7.9×10^{-4} counts s^{-1} arcmin^{-2}, $B_X v(\theta)$ summed over θ and weighted by area gives the above mean background rate for photons.

Finally, we would like to compute $n(\sigma)$ in different radial zones on the IPC. Different normalization constants are
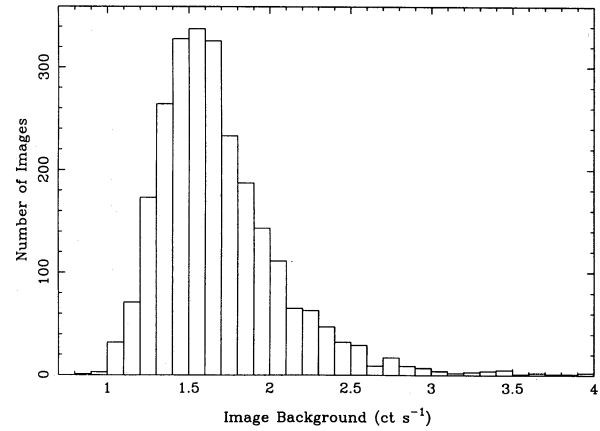

Fig. 7.—Histogram of total source-subtracted background count rates for IPC images used to construct the Two-Sigma Catalog.

therefore necessary for the different zones, and we replace the constant N_0 with $C(\theta)$. Thus, equation (5) transforms to the following:

$$\begin{aligned} n(\sigma,\theta) &= \sum_t (\alpha C(\theta) f(t) [2tv(\theta)]^\alpha \\ &\quad \times [\![\sigma^2 + \{\sigma^4 + 4[B_X v(\theta) + B_P]t\sigma^2\}^{1/2}]\!]^{-\alpha-1} \\ &\quad \times [\![2\sigma + \tfrac{1}{2}\{\sigma^4 + 4[B_X v(\theta) + B_P]t\sigma^2\}^{-1/2} \\ &\quad \times \{4\sigma^3 + 8[B_X v(\theta) + B_P]t\sigma\}]\!]). \quad (6) \end{aligned}$$

Plots of $n(\sigma, \theta)$ together with the signal-to-noise distribution for sources in the Two-Sigma Catalog are displayed in Figure 8, for 5′ wide annuli centered on the optical axis of the IPC. In Figure 8 we have omitted 3350 sources detected in fields with total background count rates in excess of 2.3 counts s^{-1}, since we have assumed a constant value of 1.6 counts s^{-1} in the calculations. The normalization constants $C(\theta)$ were determined by numerically integrating equation (6) over the limits $[5, \infty]$ for each annulus and setting the result equal to the actual number of cataloged sources above 5 σ in that annulus.

At off-axis angles greater than 5′ the signal-to-noise distributions of sources in Figure 8 are fitted very well by the model, above 4 σ in each radial range. Targets of the IPC observations contaminate the distribution in the first panel of Figure 8, causing the normalization determined by the number of sources with significance above 5 σ to be too high. However, this provides added confidence that the model fits off-axis, where sources were detected serendipitously, are accurate. Between 3.5 and 4 σ an obvious break occurs in the source signal-to-noise distributions. At the lower values of σ, it is clear that the departure of the data from the model, for a given σ, increases as the off-axis angle is increased. Thus, our inference above that the fraction of spurious sources increases with θ is confirmed. The break occurs right near the detection thresholds used in the EMSS and Deep Survey reanalysis, adding support to those investigators' choices for the signal-to-noise threshold σ_{th}.

The results of the modeling indicate that 28%, or $\sim 13,000$, of the entries in the Two-Sigma Catalog are celestial X-ray sources, assuming all the sources above 4 σ are real. Below 4 σ, this fraction is 22%. We are not bound by our initial choice of 2 σ for the catalog's signal-to-noise threshold, and our estimates of the reliability of the catalog as a function of both σ and θ permit us to apply σ thresholds which vary with off-axis angle. This is certain to
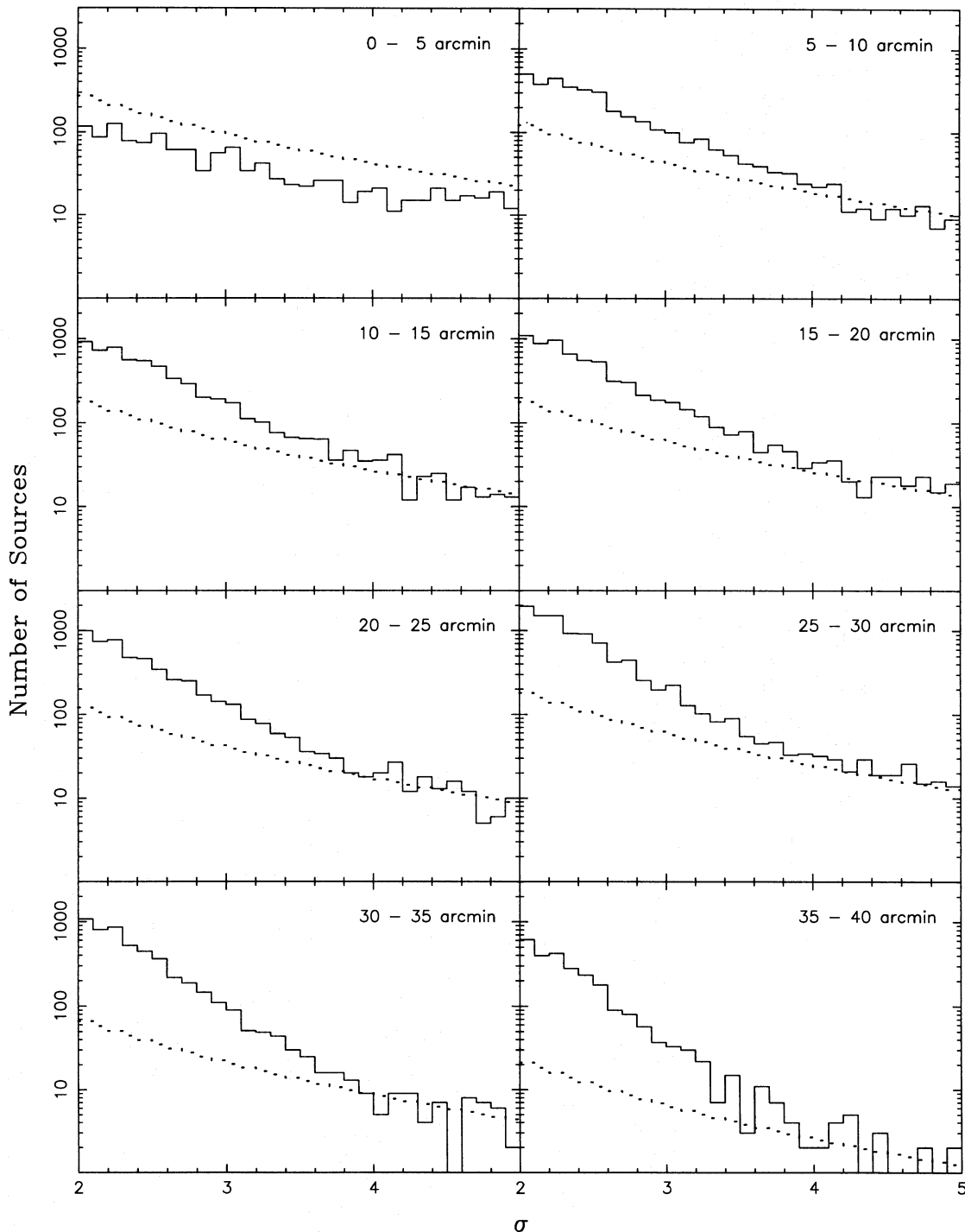
Fig. 8.—Distribution of source signal-to-noise ratios σ for the Two-Sigma Catalog, in different off-axis angle ranges (*solid lines*), and the model calculations given by eq. (6) (*dotted lines*). The model, which is in excellent agreement with the data above 4 σ, assumes the soft X-ray log N–log S relation has a slope of 1.5 in the flux range spanned by the catalog. The departure of the data from the model below 4 σ reflects the increasing number of spurious sources in the catalog at lower significances. Note the departure becomes more severe at large off-axis angles. The results of the model suggest that $\sim 28\%$, or $\sim 13,000$, of the sources in the Two-Sigma Catalog are real celestial X-ray sources.

improve the reliability of any results obtained with the catalog. We could, for example, require that at a given off-axis position at least 20% of the sources at every value of σ be real and adjust σ_{th} accordingly. Thus, we would set $\sigma_{th} = 2.0$ at $\theta < 15'$, $\sigma_{th} = 2.3$ for $15' < \theta < 20'$, $\sigma_{th} = 2.5$ for $20' < \theta < 25'$, and so on. With such adjustments to σ_{th}, the number of real sources in the catalog drops only to $\sim 10,500$, whereas the *fraction* of sources which are real climbs to 45%. Adjustments of this sort can be used in

combination with other methods for selecting out the celestial X-ray sources in the catalog; we describe the use of filters to enhance substantially the number of real sources in a subsample in the following section.

4. APPLICATIONS: SELECTION AND STUDY OF THE "REAL" TWO-SIGMA IPC SOURCES

Having characterized in detail the Two-Sigma Catalog, we can now use it for astronomical purposes. The primary

challenge lies in the determination of which 28% of the entries in the catalog are the real celestial X-ray sources. The catalog itself is not reliable enough to make the direct study of sources at the 2 σ level possible. We could, therefore, limit ourselves to sources detected above 4 σ to avoid spurious sources, as in the EMSS; this would provide us with ∼1400 new X-ray sources, after omission of the targets and previously identified EMSS sources. However, all such sources will have fluxes at or above the EMSS sensitivity threshold, and we would have the arduous task of seeking their optical counterparts in the rather large ∼1′ radius IPC position error circles. An alternative approach is to apply filters (i.e., astronomical catalogs at other wavelengths) to the Two-Sigma Catalog, in order to isolate the real celestial X-ray sources from the statistical fluctuations. The advantages of this technique are that, depending on the choice of filter, one can explore fainter X-ray sources of types not well represented in other surveys and efficiently locate their optical counterparts. The disadvantage of this procedure is that a certain amount of contamination due to chance coincidences and false X-ray sources is admitted, but the level of contamination is easily determined. Since it took over 10 years to complete 96% of the optical identifications of the 835 EMSS sources, we have opted for the second approach. As will be discussed below, large samples of X-ray sources that are ∼90% reliable can be obtained this way, even though the catalog itself contains only 28% real sources. The filters we have used are catalogs from surveys of the radio and infrared sky.

The principal motivation for studying new populations of faint X-ray sources is to search for new components of the cosmic X-ray background (XRB). The XRB is now thought to arise from the integrated emission of faint discrete X-ray sources (Mather et al. 1990). However, known classes of luminous extragalactic X-ray sources, such as quasars, Seyfert galaxies, and galaxy clusters, have failed to demonstrate the spectral and spatial properties required to account for the origin of the XRB (Fabian & Barcons 1992). Two promising candidates at this time are star-forming galaxies (e.g., Griffiths & Padovani 1990) and obscured Seyfert galaxies (e.g., Madau, Ghisellini, & Fabian 1994; Comastri et al. 1995). An excellent means for isolating both of these types of galaxies is by infrared selection. Therefore, we have cross-correlated the IPC Two-Sigma Catalog with the *IRAS* Faint Source Catalog (FSC). In addition, although radio-loud objects are not expected to make a major contribution to the XRB, we have cross-correlated the Two-Sigma Catalog with the Green Bank 6 cm Northern Sky Catalog (Becker, White, & Edwards 1991) and the Texas 80 cm interferometric catalog (J. Douglas 1991, private communication). As we discuss below, fascinating X-ray sources not represented in the EMSS have been found in both the radio and infrared samples.

4.1. *Radio Selection*

Correlations between radio and X-ray emission have been observed spanning several orders of magnitude in luminosity, for a wide variety of objects, including elliptical and S0 galaxies (Fabbiano, Gioia, & Trinchieri 1989), 3CR radio galaxies (Fabbiano et al. 1984), and quasars (Worrall et al. 1987). The correlations are usually strongest for the nuclear (or "core") radio power and the soft X-ray luminosity. Complete radio information exists for the EMSS AGNs, which has been used to compare the properties of radio-loud and radio-quiet AGNs (Della Ceca et al. 1994).

Hamilton & Helfand (1993) found a significant correlation between submillijansky radio sources and fluctuations greater than 2 σ in deep *Einstein* IPC images, concluding that star-forming galaxies, which make up the majority of sources at these radio fluxes, could contribute significantly to the soft X-ray background. However, Boyle et al. (1993), in a similar study involving a deep *ROSAT* image, found only a marginal correlation between X-ray and radio sources. This debate, plus the finding by Brinkmann, Siebert, & Boller (1994) that a considerable number of Molonglo radio sources contained in the *ROSAT* All-Sky Survey sources are radio- and X-ray–bright but optically faint, has motivated us to examine the properties of radio-selected sources in the Two-Sigma Catalog. We have utilized high- and low-frequency samples of radio sources. An advantage of using radio selection for X-ray sources is that radio positions can be determined to arcsecond precision, which greatly simplifies the identification of their optical counterparts.

4.1.1. *Cross-Correlation Statistics and Follow-up VLA Observations*

The Green Bank 6 cm catalog derived by Condon, Broderick, & Seielstad (1989) was compiled by Becker et al. (1991). The catalog contains 53,522 sources at declinations in the range $0° \leq \delta \leq 75°$, with a flux limit of 40 mJy at the equator and 20 mJy at the highest declinations. The positions of the 6 cm sources are accurate to 50″ (2 σ). Positions of sources in the unpublished Texas 80 cm catalog (J. Douglas 1991, private communication) can be accurate to ∼5″, but are sometimes ambiguous because of the interferometer's sidelobes. The flux limit of the Texas catalog, which contains 67,751 sources, is 250 mJy and the catalog covers the declination range $-25° < \delta < 72°$. Texas sources are assigned quality flags which can be used to select those sources with the most accurately measured positions and fluxes.

The results of the cross-correlations between the *Einstein* Two-Sigma Catalog and the 6 and 80 cm radio catalogs are displayed in Figures 9a and 10a, respectively. The number of matches as a function of the X-ray/radio position offset, normalized by the solid angle of the annulus represented in each offset bin, are plotted. The reason for plotting the offset distribution in this manner is that two uncorrelated catalogs will have a constant solid angle-normalized number in each offset bin; correlations are revealed by peaks above this constant level at small offsets, and the constant level establishes directly the chance coincidence rate. In both Figures 9a and 10a strong correlations are observed. To verify that the constant level in each plot accurately represents the chance coincidence rate, we shifted the positions of the radio catalog sources by some arbitrary amount, say 15′, and reperformed the matches. This process simulates the results obtained for two uncorrelated catalogs, and, as indicated by the dashed lines in Figures 9 and 10, confirms the chance coincidence level in each graph.

The chance coincidence fraction is known at every position offset. Therefore, our sample of radio-selected X-ray sources can be defined on the basis of a desired level of reliability by accepting only those matches with offsets smaller than some limit. If we choose our offset limit to be 60″ in both cross-correlations, we find that 598 X-ray sources match 6 cm radio sources with an 87% "real rate" (i.e., 13% are chance coincidences), and that 589 X-ray sources match 80 cm radio sources at a real rate of 85%. To
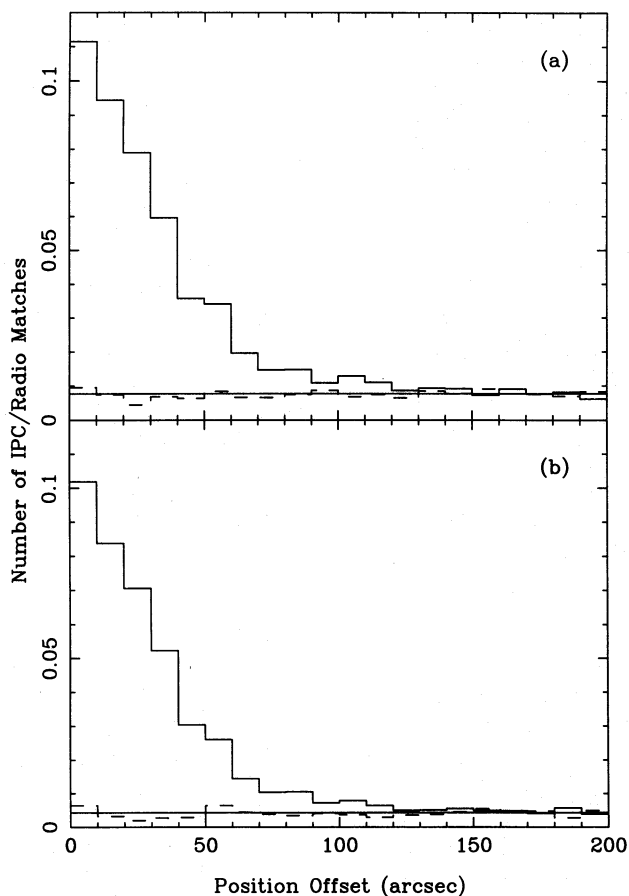
FIG. 9.—Results of the cross-correlation of the Two-Sigma Catalog with the Greenbank 6 cm radio catalog, (a) before and (b) after application of the off-axis angle-dependent signal-to-noise threshold described in the text. The dashed line indicates the chance coincidence level in each case. The solid horizontal line is the mean chance coincidence level. The number in each offset bin has been normalized by the solid angle (in arcsec^2) of the annulus that represents the offset range covered by the bin.

illustrate the usefulness of applying a position-dependent signal-to-noise threshold, σ_{th} (described above in § 3.2), if we require that at least 20% of the X-ray sources at every σ and off-axis angle be real, we remove more than 23,000 sources from the Two-Sigma Catalog, only 2,500 of which are expected to be real. Upon reperforming the cross-correlation, the number of matches of radio sources to X-ray source falls to 516 and 502 for 6 and 80 cm catalogs, respectively, for X-ray/radio position offsets of 60″ or less. However, as indicated by Figures 9b and 10b, the chance coincidence level drops significantly: 92% of the 6 cm coincidences are expected to be real, and 91% of the 80 cm coincidences are expected to be real. The chance coincidence level in each cross-correlation is determined by the relative surface densities of sources in the catalogs being compared. Thus, the removal of 50% of the X-ray sources in the Two-Sigma Catalog, most of which are spurious, is the reason the chance coincidence rates have decreased so dramatically.

Snapshots of a large fraction of the radio sources (from both samples), in the right ascension range 0^h–13^h, were made using the VLA in A array at 20 cm. We obtained additional snapshot observations for sources at other hour angles during short intervals when the VLA configuration was being changed. The snapshots, which were typically of 1 minute duration, with limiting sensitivities well below

that of either the Green Bank or the Texas survey, provided us with radio source positions accurate to ~1″. These positions were then used to make optical finding charts from the digitized Sky survey plates. Additional finding charts were made using the positions of 357 Texas 80 cm sources (not observed with the VLA) with the highest quality position and flux flags. Approximately half of the finding charts show optical counterparts above the POSS plate limit ($m < 20$), many of which are bright enough to observe spectroscopically using 2–3 m class telescopes. After checking those with optical counterparts for prior classification, we proceeded to the telescope to classify previously unidentified X-ray/radio sources.

4.1.2. *Optical Spectroscopy of Unidentified IPC/Radio Sources*

Optical spectroscopy of radio-selected *Einstein* sources was conducted primarily in three observing runs. In 1991 November, using the 3 m Shane telescope at Lick Observatory, we obtained spectra in the wavelength range 3800–8100 Å, with 7 Å (FWHM) resolution. The second two runs, using the KPNO 2.1 m telescope and Goldcam spectrograph in 1992 July and August, provided spectra over the 3700–7400 Å range at 4.5 Å resolution. A few other spectra were obtained with the Lick 3 m and the KPNO 4 m telescopes during runs dedicated to other programs, with spectrograph setups similar to those described above. Forty spectra were compiled in all.

The X-ray, radio, and optical data for the IPC/radio sources we observed are listed in Table 1. The radio source
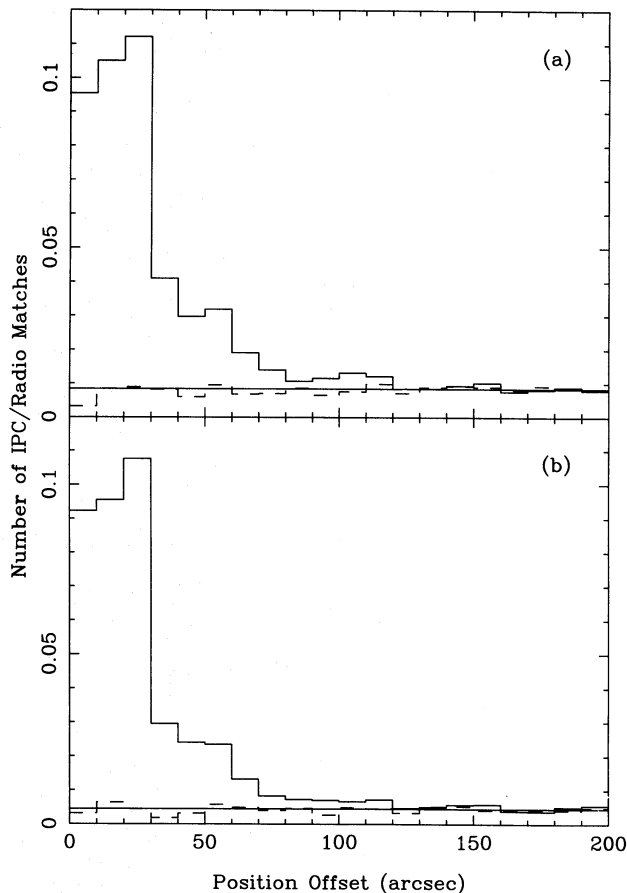

FIG. 10.—Results of the cross-correlation of the Two-Sigma Catalog with the Texas 80 cm radio catalog, (a) before and (b) after application of the off-axis angle-dependent signal-to-noise threshold.

TABLE 1

RADIO-SELECTED X-RAY SOURCES

Object	z	Classification	S_6	S_{20}	S_{80}	$\log P_6$	N_H	Seq. #	σ	C_X	F_X	$\log L_X$	$\Delta_{R/X}$	Notes
0014 + 3152	1.100	QSO	110	417	1531	27.14	5.42	2718	3.13	0.0108	4.7	45.77	45.9	1
0035 + 1211	0.090	E	75	...	...	24.46	4.28	7508	4.14	0.0133	4.9	43.27	28.5	
0049 + 0019	0.400	QSO	68	...	...	25.83	3.43	8454	4.66	0.0087	3.3	44.52	47.7	
0053 − 0952	0.101	BL Lac	56	...	341	24.43	3.93	8992	5.86	0.0203	7.3	43.55	59.5	2
0111 − 0014	0.389	NLRG	175	352	916	26.21	3.41	203	5.43	0.0160	6.1	44.75	32.0	3
0126 + 0725	0.090	Sey	32	...	...	24.09	4.25	454	4.06	0.0167	6.1	43.37	56.5	4
0137 + 5036	...	...	30	...	...	...	16.7	3351	2.42	0.0063	1.5	...	43.2	5
0145 + 3438	0.857	QSO	55	...	...	26.55	4.68	8366	6.10	0.0079	3.3	45.33	1.1	
0202 + 2332	0.176	E	101	236	639	25.20	7.07	852	2.80	0.0033	1.4	43.34	40.0	
0230 + 3429	0.458	BL Lac	220	233	...	26.48	5.80	5142	3.89	0.0080	3.6	44.69	34.2	
0458 + 6530	...	BL Lac	37	...	...	...	14.6	456	17.85	0.2420	127.2	...	15.3	
0655 + 6940	1.971	QSO	314	215	...	28.32	4.76	3441	2.76	0.0120	5.0	46.52	36.6	
0713 + 3647	0.070	E	148	334	616	24.52	6.89	3554	3.04	0.0090	3.8	42.93	31.2	2
0724 + 1555	...	...	62	255	1145	...	7.23	7334	3.30	0.0043	1.0	...	29.5	5
1033 + 0021	0.097	BLRG	242	563	576	25.03	4.88	8961	2.81	0.0143	5.4	43.38	22.3	3
1126 + 2342	3.04	QSO	104	149	340	28.42	1.34	331	3.14	0.0078	2.2	46.74	8.3	
1136 + 2814	0.830	QSO	56	...	354	26.52	1.89	6348	2.71	0.0034	1.1	44.82	25.0	
1200 + 2812	0.672	QSO	100	130	...	26.54	1.74	4258	4.34	0.0122	3.7	45.11	21.0	
1201 + 2814	0.141	NLRG	67	...	410	24.82	1.73	4258	3.15	0.0059	1.7	43.22	13.8	6
1330 + 1721	0.609	QSO	94	131	...	26.41	1.81	4023	2.10	0.0065	2.0	44.74	32.0	
1508 + 5714	4.30	QSO	279	149	191	29.34	1.55	9143	6.08	0.0216	6.4	47.70	22.2	
1559 + 0847	0.188	E	47	...	...	24.93	3.68	10438	3.89	0.0072	2.5	43.66	16.5	
1600 + 0908	0.488	QSO	103	180	501	26.21	3.75	10438	8.03	0.0253	10.0	45.20	31.7	
1606 + 2836	0.050	Sey	106	189	...	24.08	3.43	5719	3.55	0.0054	1.9	42.33	53.8	7
1613 + 0913	0.171	E	48	173	...	24.84	4.13	4109	2.27	0.0132	4.8	43.85	25.7	
1619 + 0614	0.343	E	102	307	1153	25.85	4.70	4103	2.79	0.0101	3.8	44.42	24.6	3,8
1648 + 5330	0.029	LINER	146	181	222	23.74	2.75	7829	3.14	0.0113	3.6	42.13	55.5	9
1707 + 2241	0.464	QSO	159	492	2166	26.35	4.83	4933	2.15	0.0046	1.9	44.43	33.2	3
1720 + 2501	2.25	QSO	372	669	434	27.88	4.70	420	2.40	0.0099	4.1	46.61	32.8	
1745 + 6228	3.87	QSO	574	764	1852	28.56	3.35	8869	2.59	0.0205	7.7	47.63	34.1	
1755 + 6237	0.027	Sey1.9	128	...	784	23.62	3.27	8896	3.28	0.0340	12.7	42.61	42.0	
1832 + 6845	0.205	Cl/BL	64	189	452	25.15	6.06	8651	5.60	0.0538	12.9	44.46	15.0	10
1922 + 4748	1.52	QSO	317	388	734	27.99	7.47	4617	2.16	0.0027	1.3	45.60	0.7	
2121 + 2459	1.25	QSO	109	...	...	27.29	8.73	5712	4.98	0.0075	3.7	45.82	49.9	
2130 − 0527	0.329	QSO	91	171	355	25.76	4.03	4441	2.98	0.0152	6.1	44.59	39.8	
2248 + 2441	0.056	Sey1.9	...	...	...	...	5.28	7681	3.74	0.0050	1.2	42.23	29.8	11
2318 + 0814	0.124	E	60	...	347	24.65	4.87	2598	3.18	0.0053	2.0	43.17	39.4	
2324 + 4222	0.067	E	20	...	124	23.62	9.67	3361	3.71	0.0155	7.1	43.17	52.5	12
2354 + 4709	0.045	E	566	1646	671	24.71	9.54	4618	3.27	0.0063	2.9	42.42	2.5	3
2357 + 4650	0.575	QSO	83	...	...	26.29	9.62	4618	3.49	0.0086	4.4	45.02	17.6	

NOTES.—(1) A B2 radio source; not a known X-ray source when we observed it. X-ray detection recently published (Wilkes et al. 1994). (2) Weak [N II] emission line. (3) A 4C radio source. (4) Chance coincidence? Radio source coincident with E galaxy (at same z) 20″ northwest of weak-lined AGN. (5) Optical object observed is a faint star. Probable chance coincidence. (6) In cluster Abell 1451. Weak emission lines. (7) IC 4590. Weak emission lines, E galaxy continuum. (8) Hα region not observed; classification tentative. (9) In group of galaxies (Arp 330); X-ray emission could be extended. (10) Hα measurement needed to firmly establish classification. Very strong [O II]; possible cluster or BL Lac object. (11) Chance coincidence. A VLA image shows that the galaxy is a weak radio source, but a much stronger compact radio source is located 15″ to the northeast. (12) A B3 radio source.

catalog names (relating to their B1950.0 coordinates), the redshifts z, and classifications determined from our spectra are given in the first three columns. To clarify a few of the classifications used, broad- and narrow-line radio galaxies are denoted BLRG and NLRG, Sey and LINER are used for Seyfert and low-ionization nuclear emission-line region galaxies, E denotes an early-type galaxy spectrum devoid of strong emission lines, and Cl/BL is used for the one object which could be a cluster or a BL Lac object. The 6, 20, and 80 cm radio flux densities (in mJy) appear next, followed by the 5 GHz radio power (in W Hz^{-1}) for each object. Radio fluxes at 20 cm are taken from the Green Bank 20 cm Northern Sky Catalog of White & Becker (1992). For objects with 80 cm flux densities only, S_6 was estimated by extrapolating from the 80 cm measurement, assuming a power-law spectrum with index $\alpha = 0.7$. The Galactic H I column (in units of 10^{20} cm^{-2}) in the direction of each object (Stark et al. 1992), the IPC sequence number, the signal-to-noise ratio of the X-ray detection, and the IPC count rate are provided in the next four columns of Table 1. The X-ray fluxes ($\times 10^{-13}$ ergs cm^{-2} s^{-1}) in the 0.16–3.5

keV IPC band, which follow, assume a 1 keV thermal spectrum for normal galaxies or a power law with photon index $\Gamma = 2$ for AGNs, in addition to the tabulated Galactic N_H value. The X-ray luminosity L_X (in ergs s^{-1}) was computed assuming $H_0 = 50$ km s^{-1} Mpc^{-1} and $q_0 = 0$. The radio/X-ray position offsets (in arcsec) are listed last.

The classification of our quasars was straightforward. Classifications of other emission-line spectra were made on the basis of the emission-line flux ratios and velocity widths (Veilleux & Osterbrock 1987), incorporating the radio luminosity information. Seyfert galaxies usually have radio powers at 20 cm below a few times 10^{24} W Hz^{-1} (Ulvestad & Wilson 1989); therefore, we adopt a limit of 10^{24} W Hz^{-1} at 5 GHz to distinguish radio galaxies from the lower radio power Seyferts and LINERs. BL Lac objects were classified using the criterion established by Stocke et al. (1991), that the Ca II break "contrast" be less than 25%. For one BL Lac, the 18 σ X-ray source 0458 + 6530, we could not determine a redshift. None of the early-type galaxies in our list appear to be members of galaxy clusters on the POSS images, including the one (1201 + 2814) supposedly situated

in the cluster Abell 1451 (which previously did not have a published redshift). We discuss below the possibility that some of our early-type galaxies are actually in clusters.

Table 1 indicates that most of the objects we observed are exactly what we would expect to find in a radio- and X-ray–selected sample: quasars (17), broad- and narrow-line radio galaxies (3), BL Lac objects (3), lower luminosity AGNs (5), and radio-loud early-type galaxies (10) (see Tananbaum et al. 1979; Fabbiano et al. 1984; Morris et al. 1991; Fabbiano et al. 1989). In two cases, the optical object closest to the radio position turned out to be a star; we did not search the $\sim 1'$ radius IPC error circle for more plausible counterparts to the X-ray sources in these instances. One early-type galaxy ($1832 + 6845$ at $z = 0.205$) is tentatively classified as a cluster/BL Lac object. It has an elliptical galaxy continuum with an extremely strong [O II] $\lambda 3727$ line and only weak [O III] $\lambda 5007$ and Hβ emission, characteristics which typify galaxies in cooling flow clusters (see Allen et al. 1992). An associated cluster, however, is not apparent on the POSS finding chart.

A closer look at Table 1 reveals two surprises: (1) the presence of high-redshift ($z > 3$) quasars, which are absent in the EMSS, and (2) the large number of early-type galaxies with little or no evidence for emission lines in their spectra, yet with X-ray luminosities comparable to those of broad-line AGNs (i.e., $L_X > 10^{42}$ ergs s^{-1}). We discuss these two interesting subgroups further here.

4.1.2.1. High-Redshift Quasars

X-ray studies of high-redshift quasars provide information regarding the environs, evolution, and inherent properties of the most luminous AGNs (Elvis et al. 1994; Bechtold et al. 1994b; Pickering, Impey, & Foltz 1994). At this time, however, only ~ 20 X-ray–detected quasars with $z > 3$ are known; thus, each new example adds an important datum for such investigations. One of the first objects observed as part of this project was $1745 + 6228$, a quasar at $z = 3.87$ (Becker, Helfand, & White 1992). Since then, we have observed two other high-z quasars with redshifts of 3.04 and 4.30. Thus, 3/40 of the radio-selected *Einstein* sources we have observed are high-redshift quasars. By contrast, the highest redshift object of the 835 EMSS sources is a $z = 2.83$ quasar. Our use of radio selection may have contributed to this striking difference. On the other hand, our examination of the data at fainter flux levels, and our development of a more sensitive detection procedure, must also be partly responsible.

The $z = 4.30$ quasar $1508 + 5714$ is the second most distant X-ray source now known, just eclipsed by a recently discovered quasar at $z = 4.32$ (Henry et al. 1994). It was detected in IPC sequence number I9143 as a 6.1 σ source, and we obtained its spectrum in 1994 May at the KPNO 4 m telescope (see Fig. 11). The quasar $1508 + 5714$ was discovered independently by Hook et al. (1995), who selected it solely on the basis of its radio properties. The reason the quasar is not already a known X-ray source is a mystery. The source is clearly visible (three contours above background) in the image of I9143 published in SAOs *Einstein Observatory* Catalog of IPC X-Ray Sources (Harris et al. 1990), but apparently fails to exceed the signal-to-noise limit of 3.5 σ used in that catalog. We can only surmise that our use of a locally determined background and application of the IPC flat field have afforded us a more accurate mea-
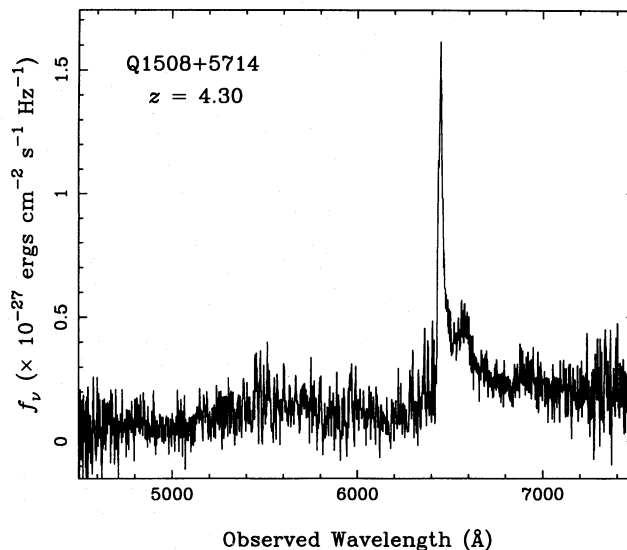

FIG. 11.—Discovery spectrum of Q1508+5714, the $z = 4.30$ radio-bright and X-ray–bright quasar. The strong line is Lyα.

surement of the background level in the image, and thus a better detection.

We measure a background-subtracted IPC count rate of 0.027 counts s^{-1} for $1508 + 5714$, which makes it the fourth highest flux X-ray quasar with $z > 3$, and the brightest (and most luminous) X-ray quasar above a redshift of 3.4. In Table 2 we have assembled what we believe to be a complete listing of all published X-ray–detected quasars with redshifts in excess of 3. This includes our $z = 3.04$ quasar, $1126 + 2342$. Because many of the quasars in Table 2 have

TABLE 2
X-Ray-detected High-z Quasars

QSO	z	Radio Loud?	C_X[a]	Reference
$1126 + 2342$	3.04	Yes	15.6	1
$1508 + 5714$	4.30	Yes	54.0	1
$1745 + 624$	3.87	Yes	23.1	1,2,3
$1759 + 6638$	4.32	No	1.1	4
$0000 - 263$	4.11	No	4.3	5
$0014 + 813$	3.38	Yes	67.0	5
$0130 - 403$	3.03	No	8.1	5
$0420 - 388$	3.12	No	30.9	5
$0636 + 680$	3.17	Yes	12.9	5
$1208 + 101$	3.82	Yes	5.0	5
$1946 + 768$	3.02	No	6.8	5
$2000 - 330$	3.78	Yes	16.9	5
$2126 - 158$	3.27	Yes	170.3	5
$0041 - 2638$	3.05	No	4.4	6
$0042 - 2627$	3.29	No	5.7	6
$0256 - 0000$	3.36	Yes	7.4	6
$2231 - 0015$	3.02	No	8.3	6
$0537 - 286$	3.11	Yes	60.7	7
$0642 + 449$	3.40	Yes	43.3	7
$1402 + 044$	3.20	Yes	6.6	7
$1614 + 051$	3.21	Yes	9.6	7
$2204 - 408$	3.18	Yes	12.1	7

[a] Measured or estimated *ROSAT* PSPC count rate $\times 10^{-3}$ counts s^{-1}.

REFERENCES.—(1) This work; (2) Becker et al. 1992; (3) Fink & Briel 1993; (4) Henry et al. 1994; (5) Bechtold et al. 1994a; (6) Pickering et al. 1994; (7) Worrall et al. 1987.

been observed with *ROSAT*, we have listed Position Sensitive Proportional Counter (PSPC) count rates. For those quasars with IPC detections only, we have estimated the PSPC count rate by multiplying the IPC count rate by a factor of 2, which is appropriate for most X-ray sources (see Appendix F of the *ROSAT* mission description). Note that $1508 + 5714$ is 50 times brighter than the $z = 4.32$ quasar and thus provides the only feasible opportunity to examine in detail quasar X-ray emission at $z > 4$. We have recently carried out an *ASCA* observation of $1508 + 5714$ to study its X-ray properties in the 2–60 keV (rest) range.

There is a putative dearth of radio-loud quasars at high redshifts, which has prompted the suggestion that radio-loud and radio-quiet quasars have evolved differently (Schmidt et al. 1995). The three high-z quasars in our sample are, by definition, all radio-loud; in fact, $1508 + 5714$ and $1745 + 6224$ are currently the highest redshift radio-loud quasars known. It would appear, based on the frequency of such quasars in our list, that X-ray selection is an efficient means for finding high-z radio-loud quasars.

4.1.2.2. High-L_X Normal Early-Type Galaxies

One of the surprises uncovered during the EMSS optical identification process was several normal elliptical galaxies with X-ray luminosities $L_X \approx 10^{43}$ ergs s^{-1} (Stocke et al. 1991), an order of magnitude more luminous than early-type galaxies surveyed previously with *Einstein* (Fabbiano et al. 1989). Radio- and X-ray–loud, but optically undistinguished, galaxies are also present among Molonglo 408 MHz Survey radio sources detected in the *ROSAT* All-Sky Survey (Brinkmann et al. 1994). We have found several similar "optically passive" X-ray galaxies: eight of the 40 objects listed in Table 1 have normal early-type galaxy classifications and X-ray luminosities which range from 10^{43}–$10^{44.5}$ in the 0.16–3.5 keV band, typical of broad-line AGNs. Our galaxies differ from those contained in the EMSS in that they are all fairly radio-loud ($P_{5\,GHz} > 10^{24}$ W Hz^{-1}), whereas the EMSS galaxies, with lower average redshifts than ours, are mostly undetected at 6 cm ($S_6 < 1$ mJy). However, this difference may simply be an artifact of our radio selection, and the X-ray emission mechanisms may be the same in the two sets of galaxies.

The most obvious possibilities for the nature of these X-ray–luminous early-type galaxies is that they are either optically weak BL Lac objects, in which starlight dominates the continuum, or radio galaxies situated in X-ray–emitting clusters. As discussed above, we have already examined the Ca II break contrast in the spectra of these objects. The eight galaxies in question here all have break contrasts typical for normal early-type galaxies, but this does not rule out some BL Lac activity. Therefore, we obtained deep VLA and CCD images for five of the galaxies to test further the BL Lac and cluster hypotheses. The CCD images indicate that while none of these galaxies is in a rich cluster, all have nearby galaxian companions at small projected separations. Similarly, the VLA images reveal that none of the galaxies have the extended, distorted radio tails common to radio galaxies in the cluster environment. On the other hand, the radio emission is not dominated by an unresolved, compact core in any of the galaxies, which convincingly rules out BL Lac activity (Kollgaard et al. 1992). Instead, the radio morphologies of these galaxies are amorphous or double-lobed with signs, in two cases, for a weak core component. The radio emission appears to be confined to the optical extent

of the galaxy. Figure 12 (Plate 4) displays the optical spectrum, optical R-band image, and VLA 20 cm radio image of $2324 + 4222$, an optically passive X-ray galaxy at a redshift of 0.068. The spectrum of $2324 + 4222$ is clearly devoid of emission lines. The compact-double radio structure has a size of $\sim 15''$ and is contained well within the optical extent of the galaxy. Several galaxies are located within 3' (~ 350 kpc) of the bright elliptical.

There are two promising alternatives for the origin of the X-rays in these objects. First, some sort of nonstandard AGN may be present. For example, the radio galaxy 3C 264 was observed to have a nuclear pointlike X-ray source in an *Einstein* HRI observation, yet its optical spectrum is remarkably dull: a starlight-dominated early-type galaxy continuum and only the slightest hint of Hα + [N II] emission lines (Elvis et al. 1981). The radio and X-ray luminosities of 3C 264, as well as its amorphous radio structure (Baum et al. 1988), are comparable to those of our objects. 3C 264 might therefore represent an AGN prototype for our optically passive X-ray galaxies. Alternatively, the X-ray emission in these objects could arise in a hot, diffuse medium associated with a small group of galaxies. Such emission has been recently discovered with *ROSAT* and, as noted above, all the galaxies for which we have CCD images have nearby companions. As an example, the X-ray emission from the galaxy group HCG 62 (Ponman & Bertram 1993) extends over at least 360 kpc and has a luminosity of 1×10^{43} ergs s^{-1} in the *ROSAT* band. We have marginal evidence that the closest of our galaxies, $2324 + 4222$ (shown in Fig. 12), is extended in the IPC image: the signal-to-noise ratio of the detection of this source increases steadily as the aperture within which photons are collected is increased from 1 (S/N = 3.71 σ) to 2 (S/N = 4.05 σ) to 3 (S/N = 4.42 σ) times the size of an IPC point source. ROSAT HRI observations, scheduled for three of the brightest sources, will determine whether the X-ray emission is point-like or extended in these objects. These results, along with our radio and optical images, will be published elsewhere (Moran, Helfand, & Becker 1996).

4.2. *Infrared Selection*

Infrared galaxies have also been studied extensively at X-ray wavelengths, frequently in the context of the XRB. As mentioned above, two promising candidates for the origin of the XRB are obscured Seyferts and star-forming galaxies, both of which are expected to turn up in IR-selected samples. In a search for obscured Seyfert galaxies, *IRAS* Point-Source Catalog (PSC) galaxies within *HEAO 1* error boxes were studied by Kirhakos & Steiner (1990), who found a large number of type 2 Seyfert galaxies that they interpreted to be obscured Seyfert 1s, on the basis of their hard X-ray properties. However, the identification of these *IRAS* galaxies as X-ray sources is very uncertain due to the large size (1° × 3°) of the *HEAO 1* error boxes. In the soft X-ray regime, the *Einstein* IPC and *IRAS* PSC databases have been used to establish correlations between soft X-ray and far-infrared luminosities for normal and star-forming galaxies (David, Jones, & Forman 1992), as well as for broad-line AGNs (Green, Anderson, & Ward 1992). Optical spectroscopy of 11 IPC/PSC sources by Fruscione & Griffiths (1991) further established the presence of starburst galaxies in X-ray/IR-selected samples and provided preliminary support to the hypothesis of Griffiths & Padovani
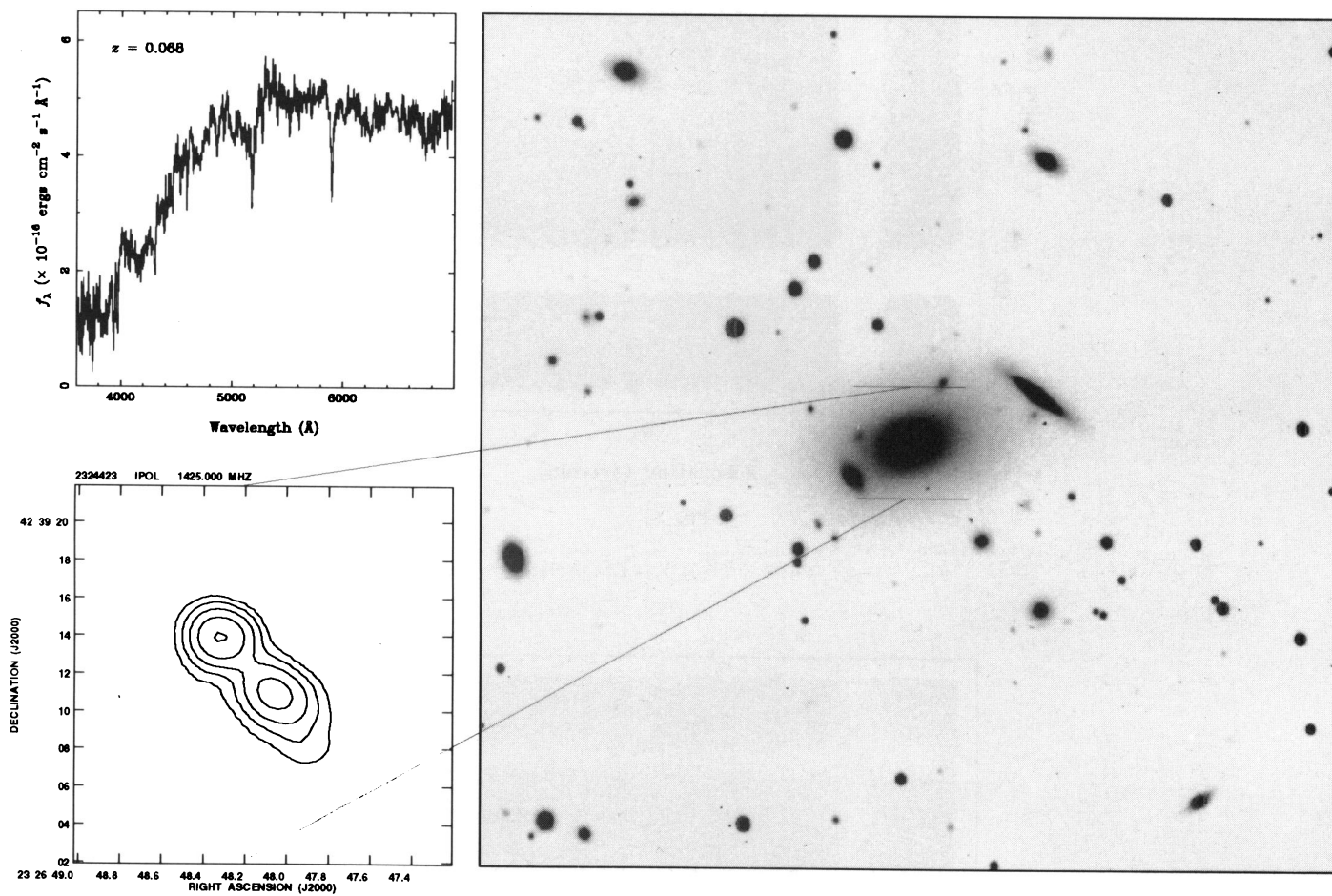
PLATE 4

FIG. 12.—Optical spectrum, 20 cm VLA A-array radio image, and 900 s *R* band optical image of the optically passive X-ray galaxy 2324+4222

MORAN et al. (see 461, 139)

(1990) that starburst galaxies might contribute significantly to the XRB.

The contribution to the intensity of the soft XRB by IR-bright galaxies has been estimated in various ways, by the above authors, to fall between 5% and 40%. Boller et al. (1992) cataloged 241 *IRAS* PSC sources detected in the *ROSAT* All-Sky Survey, of which 20 appeared to be "normal" spiral galaxies and starbursts with extreme X-ray luminosities (i.e., $L_X > 10^{42}$ ergs s^{-1}). These, too, could have interesting implications for the XRB, and we have examined the Boller et al. sample in detail (Moran, Halpern, & Helfand 1994; Moran, Halpern, & Helfand 1995). To complement these studies of X-ray–bright infrared galaxies, we have matched our *Einstein* Two-Sigma Catalog with the *IRAS* Faint-Source Catalog (FSC). Both of these catalogs are substantially deeper than the source lists employed in previous works. Most *IRAS* galaxies are optically bright and are visible on the Palomar plates; thus, given the size and position angle of the *IRAS* position error ellipse, it is usually straightforward to determine the correct optical counterpart even though *IRAS* positions can have substantial uncertainties ($\sim 1'$).

4.2.1. *Cross-Correlation Statistics*

The *IRAS* FSC (Moshir et al. 1992) contains 173,044 point sources detected in at least one of the spectral bands centered at 12, 25, and 60 μm, and is a factor of ~ 2.5 more sensitive than the PSC. The FSC covers Galactic latitudes $|b| > 10°$ at 12 and 25 μm, and $|b| > 20°$ at 60 μm. As described by Moshir et al. (1992), sources likely to be galaxies or stars can be selected on the basis of their infrared colors. Thus, to choose the "galaxies," we selected the FSC sources detected with high–flux-density quality at 60 μm, for which $S_{12\,\mu m} < S_{60\,\mu m}$. This FSC subsample consists of 60,944 sources at least 20° from the Galactic plane.

Cross-correlation of the IPC Two-Sigma Catalog with the FSC "galaxies" subsample was performed in the same manner as that described above in § 4.1.1. The results are illustrated in Figure 13a for the full Two-Sigma Catalog. Again, a very strong correlation is observed at small offsets and is particularly significant for offsets less than 40″. The chance coincidence rate is slightly larger in this cross-correlation than it was for those with the radio catalogs. A total of 371 *IRAS* sources match IPC sources at offsets less than 60″, but at a true coincidence rate of just 76%. At offsets less than 40″, there are only 254 matches, but the fraction of true coincidences climbs to 86%. The application of an off-axis angle-dependent significance threshold, σ_{th}, decreases the chance coincidence rates considerably. As above, we required that at each off-axis angle at least 20% of the sources in any σ-interval not be spurious, and reperformed the cross-correlation, the results of which are displayed in Figure 13b. At offsets less than 60″, there are now only 309 total matches, but the fraction of true coincidences has increased to 83%. At offsets less than 40″, 90% of the 222 coincidences are expected to be real. Optical finding charts were made for the full sample of 371 *IRAS/Einstein* sources using the *IRAS* source positions. The position error ellipses associated with each source were used to determine the likely optical counterparts to the *IRAS* sources.

4.2.2. *Optical Spectroscopy of Unidentified IPC/FSC Sources*

Optical spectra of unidentified IPC/FSC sources were obtained primarily in two observing runs at the Lick 3 m
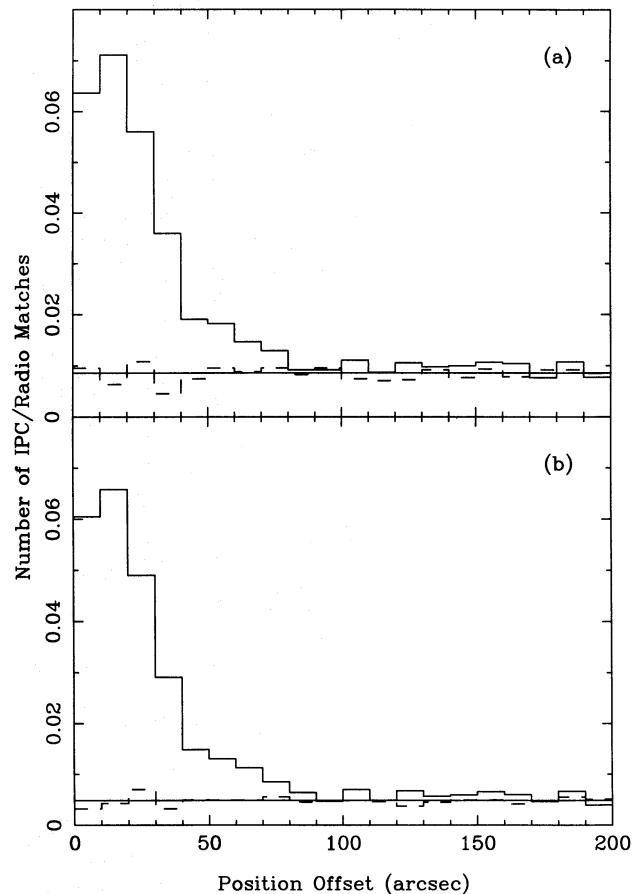

FIG. 13.—Results of the cross-correlation of the Two-Sigma Catalog with the *IRAS* Faint Source Catalog (a) before and (b) after application of the off-axis angle-dependent signal-to-noise threshold.

telescope in 1993 July and December, using the Kast Double Spectrograph. These spectra cover the wavelength range 3400–8100 Å at 5 Å (FWHM) resolution. Additional spectra with comparable wavelength coverage and spectral resolution were obtained at the KPNO 2 m and 4 m telescope. A total of 53 objects were observed; 37 of these survive the application of the off-axis, angle-dependent signal-to-noise thresholds described above and therefore represent the most reliable coincidences in our list. We consider only these 37 X-ray–detected infrared sources below. None of the objects observed was a previously known X-ray source; 10 had published redshifts (mainly from redshift surveys only) but lacked specific classifications. The redshifts of these 10 objects implied interesting X-ray luminosities (i.e., L_X greater than a few times 10^{41} ergs s^{-1}), so we observed them to establish correct classifications. An eleventh galaxy, 12134+1257 (=Mrk 764) was classified previously as a starburst galaxy by Balzano (1983), but its published redshift indicates an X-ray luminosity of $L_X = 5.2 \times 10^{42}$ ergs s^{-1}. Our observation shows it to be a Seyfert 1.9 galaxy, more consistent with its high X-ray luminosity. The other 26 objects in our sample were previously unidentified, and none of our objects was a target of an *Einstein* observation.

Table 3 lists the X-ray, *IRAS*, and optical data for the FSC objects we observed. The FSC source name (=B1950.0 coordinates), the redshift, and our spectral classification of each object comprise the first three columns. The 60 and 100 μm *IRAS* flux densities from the FSC (in Jy) and the

TABLE 3

INFRARED-SELECTED X-RAY SOURCES

Object	z	Classification	S_{60}	S_{100}	$\log L_{\mathrm{FIR}}$	N_{H}	Seq. #	σ	C_{X}	F_{X}	$\log L_{\mathrm{X}}$	$\Delta_{\mathrm{IR/X}}$	$\Delta_{\mathrm{O/X}}$	Notes
00188 + 2214	0.0195	H II	0.403	<3.399	43.56	4.08	7765	5.90	0.0081	2.02	41.53	37.3	12	1
01105 + 0201	0.0462	Sey1.9	0.552	1.599	44.56	8.88	8458	3.19	0.0045	2.25	42.34	57.5	63	2,3
01227 + 3341	0.0280	H II	0.298	<0.616	43.74	5.11	4199	2.56	0.0045	1.73	41.78	53.1	68	
01445 + 3503	0.0655	Comp	0.232	0.510	44.44	4.72	8366	4.35	0.0064	1.78	42.54	36.2	19	
02585 − 1515	0.1159	?	0.288	1.851	45.43	4.25	9183	3.48	0.0058	1.45	42.79	37.5	70	4
04061 − 1307	0.0789	Sey1.9	0.188	<1.038	44.46	3.67	10648	2.91	0.0038	1.48	42.63	59.1	60	2
08012 + 1008	0.0343	H II	0.229	0.810	43.97	2.70	181	3.68	0.0047	1.13	41.77	16.3	24	5
08045 + 6301	0.0702	Sey2	0.221	<0.971	44.43	4.37	8357	3.06	0.0026	0.72	42.21	25.0	42	2
08083 + 6223	...	Star	0.227	1.134	...	...	8357	3.48	0.0034	...	...	33.6	41	
08255 + 2630	0.0526	Comp	0.773	<2.982	44.72	3.70	5929	3.14	0.0045	1.75	42.34	53.8	70	
09131 + 7500	0.1266	H II	0.347	<0.888	45.16	2.08	8439	2.44	0.0017	0.51	42.60	38.2	15	
09446 + 1359	0.0739	Sey1.9	0.466	0.654	44.77	3.04	4944	2.81	0.0172	4.55	43.06	28.1	11	
10200 + 4839	0.0625	H II	0.293	0.565	44.47	1.13	4614	2.13	0.0058	1.48	42.42	36.4	10	
10518 + 1801	0.0542	H II	0.516	1.048	44.60	2.58	7757	2.85	0.0042	1.01	42.13	38.2	45	6
11078 + 3614	0.0711	H II	0.389	0.887	44.75	2.13	3122	2.53	0.0050	1.50	42.54	42.0	40	6
11151 + 2934	0.0232	Sey1.8	0.317	0.864	43.70	1.53	1844	3.78	0.0205	4.89	42.06	24.5	23	
12013 − 0326	0.0127	H II	0.244	0.560	43.02	2.53	4289	2.97	0.0064	1.53	41.03	57.5	80	
12134 + 1257	0.0655	Sey1.9	0.421	0.950	44.70	2.57	4303	4.07	0.0104	2.68	42.72	29.5	14	7
12230 + 0755	0.0372	Comp	0.441	1.018	44.23	1.60	6993	5.71	0.0195	4.68	42.46	41.5	43	
13006 + 3556	0.0371	H II	2.743	4.090	44.94	1.04	5392	3.98	0.0016	0.48	41.47	41.7	87	6
13049 + 3437	0.2224	Sey2	0.438	0.912	45.83	1.04	2608	4.01	0.0105	2.37	43.79	23.1	25	
13342 + 0332	0.0231	H II	0.259	0.848	43.65	1.97	5547	3.98	0.0047	1.39	41.51	29.0	26	
14060 + 7207	0.0341	Sey1.9	0.529	1.108	44.21	1.87	10197	3.22	0.0081	1.99	42.01	34.5	34	
14203 + 3005	0.1144	Sey1.9	0.960	1.387	45.49	1.33	5557	3.03	0.0077	1.80	43.05	22.2	9	
14362 − 0657	0.0868	IZw1	0.836	0.607	45.03	5.43	5382	2.78	0.0074	3.23	43.06	32.0	37	
14445 + 1147	0.0317	LINER	0.187	0.864	43.88	1.66	10474	3.02	0.0033	0.80	41.55	41.5	25	8
15033 + 2617	0.0553	Sey2	0.237	0.716	44.37	3.40	1907	4.08	0.0038	1.02	42.15	37.1	45	2
16008 + 3339	0.0625	H II	0.200	<1.109	44.28	2.29	3986	3.06	0.0082	2.42	42.64	44.6	65	9
16022 + 1753	0.0412	LINER	0.661	1.215	44.45	3.39	3713	8.24	0.0269	10.2	42.89	12.8	37	10
16075 + 2838	0.1690	Sey	0.840	1.006	45.76	3.42	5719	2.69	0.0036	1.36	43.29	53.6	60	
16480 + 5329	0.0267	H II	0.214	<1.634	43.56	2.75	7829	3.14	0.0113	3.65	41.93	59.9	74	11
17039 + 6039	0.0968	Sey2	0.398	0.600	44.96	2.29	5688	2.65	0.0010	0.25	42.04	33.2	40	12
17079 + 7118	0.0400	H II	0.191	0.748	44.05	4.13	29	3.65	0.0013	0.47	41.52	38.6	16	
17549 + 6520	0.0803	Sey1	0.374	0.845	44.84	3.67	8749	4.82	0.0443	8.54	43.41	49.8	51	
17551 + 6209	0.0844	Sey1.9	0.388	1.017	44.93	3.37	8897	2.30	0.0146	3.92	43.12	29.6	21	
17583 + 6934	0.0795	Sey1	0.207	<1.060	44.51	3.41	8848	3.15	0.0178	4.78	43.15	35.5	41	
23489 + 0827	0.0417	Sey2	0.424	<1.775	44.25	6.12	5744	2.97	0.0053	1.50	42.04	25.0	35	

NOTES.—(1) IC 1546, weak emission lines. In galaxy group; elliptical companion ($z = 0.0208$) $\sim 1'$ west-northwest. (2) Very reddened spectrum. (3) UGC 768. (4) Faint object and noisy spectrum; classification uncertain. Weak [N II], Hα emission lines; [N II]/Hα ≈ 1. (5) Mrk 1209. (6) Close H II galaxy pair (at same z). (7) Mrk 764; classified as starburst by Balzano (1983). (8) E(?) galaxy with weak emission lines in group of galaxies; [N II]/Hα $\gg 1$. (9) Chance coincidence? Nearby M star. (10) NGC 6040 ($=$ Arp 122); S nucleus has LINER spectrum, possible broad Hα. N nucleus is reddened; possible Seyfert 2. (11) In group of galaxies (Arp 330); northern companion has LINER spectrum (see Table 1); X-ray emission could be extended. (12) Close H II companion at $z = 0.0971$.

computed far-infrared luminosity (in ergs s^{-1}) are listed in the next three columns. L_{FIR} ($=4\pi D_L^2 F_{\mathrm{FIR}}$ ergs s^{-1}) is computed using the formulae $F_{\mathrm{FIR}} = 1.26 \times 10^{-11}$ ($2.58 S_{60\mu m} + S_{100\mu m}$) and $D_L = cz(1 + z/2)/H_0$, where z is the redshift. For objects with flux density upper limits at 100 μm, we estimated S_{100} assuming $\alpha(60, 100) = -1$ in order to compute L_{FIR}. As in § 4.1.2, we assume $H_0 = 50$ km s^{-1} Mpc^{-1} and $q_0 = 0$. The Galactic H I column toward each FSC source ($\times 10^{20}$ cm^{-2}), the IPC image sequence number containing the X-ray source, the significance of the X-ray detection, and the IPC source count rate are given in the next four columns. These data were used to compute the X-ray flux (in units of 10^{-13} ergs cm^{-2} s^{-1}) and luminosity (in ergs s^{-1}) in the 0.16–3.5 keV band assuming a $kT = 1$ keV thermal spectrum for normal and H II galaxies and a power-law spectrum with photon index $\Gamma = 2$ for AGNs. Finally, the IR/X-ray and optical/X-ray position offsets (in arcsec) for each IR/X-ray coincidence are listed in the last two columns.

All of the objects we observed have emission-line optical spectra. Spectral classifications were determined using the emission-line flux-ratio diagnostics described by Veilleux & Osterbrock (1987) and Filippenko & Terlevich (1992) along with the emission-line velocity width information. Table 3 indicates that most of the objects in our sample fall into the categories of Seyfert galaxies (Sey), LINERs, and normal late-type galaxies and starburst galaxies (H II). One object observed, a bright K star, is likely to be both the X-ray and the infrared source. (Our "galaxies" subsample of the *IRAS* FSC is not completely free of stellar sources.) One of the remaining objects is a I Zw 1–type Seyfert galaxy, and three others are "starburst/Seyfert composite" galaxies, which we describe more fully below. Note that several of the objects are interacting galaxies or close galaxy pairs. Any assertions we make based on the representation of various classes in our sample are somewhat preliminary, since we have a relatively small sample that is not complete. However, there should not be any strong selection biases in this sample of serendipitously detected X-ray sources.

We expect there to be six chance coincidences among the 37 objects in our sample. In principle, the optical/X-ray position offsets $\Delta_{O/X}$ (penultimate column of Table 3), which are accurate to $\sim 5''$, could help distinguish these chance coincidences. However, the largest value of $\Delta_{O/X}$ is 87$''$, and only three objects have offsets in excess of 70$''$. Since several EMSS sources have optical/X-ray offsets this large, $\Delta_{O/X}$ for

our objects may not be particularly useful for determining the chance coincidences in the sample. The significance of the X-ray detection σ may be a more suitable discriminator.

There are apparently exceptional X-ray sources in each of the subclasses of IR- and X-ray–emitting objects, which we discuss in detail here.

4.2.2.1. Seyfert Galaxies

There are 17 outright Seyfert galaxies in our sample. Twelve indicate some degree of type 1 activity (i.e., broad permitted emission lines), and only five are type 2 Seyferts. In contrast, optically selected Seyfert galaxy samples usually find type 1 and type 2 objects in the proportion $\sim 1:3$ (e.g., Osterbrock & Shaw 1988). Our high Seyfert 1 fraction is likely due to the soft X-ray selection used (cf. Stephens 1989), and to the fact that we have considered only unclassified objects; this increases the mean redshift of our subsample and biases us against less luminous X-ray sources. One Seyfert 2, $13049 + 3437$ at $z = 0.2224$, has an extremely high X-ray luminosity ($L_X = 6 \times 10^{43}$ ergs s^{-1}). Unfortunately, the object is very faint: a better spectrum is required to provide accurate emission-line measurements and to determine whether or not the Hα line has a broad component. Included among the Seyfert 1s is a I Zw 1–type galaxy, $14362 - 0657$. Such objects, also called "narrow-line Seyfert 1s," are known to be luminous X-ray and infrared sources (Halpern & Oke 1987; Moran et al. 1995).

One of the Seyferts in our sample, $16075 + 2838$ at $z = 0.169$, has a remarkable spectrum, which we display in Figure 14. The striking aspect of the spectrum is that the forbidden [O III] lines are broader than all other lines in the spectrum, forbidden or permitted. This is a very rare circumstance in Seyfert galaxies. The velocity width of [O III] $\lambda 5007$ is 1480 km s^{-1} (FWHM), whereas the width of Hβ is only 390 km s^{-1}. There is an obvious blue asymmetry to all the emission lines, which makes it difficult to measure accurately the widths of the blended lines such as Hα, [N II], and [S II]. With this single spectrum alone we are not able to solve the puzzle of the emission-line widths. CCD imaging and higher S/N spectra at greater resolution are needed to decipher the true nature of this Seyfert galaxy.

Fortuitously, $16075 + 2838$ has been observed as part of the *FIRST* VLA survey of the radio sky (described in Becker, White, & Helfand 1995). Its 20 cm flux density is 3.8 mJy, which, at $z = 0.169$, means its 20 cm radio power is 5.5×10^{23} W Hz^{-1}. This radio luminosity is among the highest known for Seyfert galaxies (Ulvestad & Wilson 1989). A possible expanation for the width of the [O III] lines is that the radio-emitting plasma is interacting with the ambient interstellar medium in the host galaxy, giving rise to spatially extended [O III] emission with a multiplicity of velocity components. Such effects have been observed in some radio-bright Markarian galaxies (Whittle et al. 1988), the unusual Seyfert galaxy Was 49 (Moran et al. 1992), and galaxies harboring compact steep-spectrum (CSS) radio sources (Gelderman & Whittle 1994). Our spectrum contains most of the light from the galaxy; thus, if such extended [O III] emission is present, the integrated light spectrum might plausibly indicate an unusually broad [O III] velocity width. High-resolution radio images at several frequencies would provide important information about this object.

4.2.2.2. LINERs

One of the two LINERs in our sample, $16022 + 1753S$, has an X-ray luminosity exceptional for its class ($L_X = 8$

$\times 10^{42}$ ergs s^{-1}; LINER luminosities are typically 10^{42} ergs s^{-1} or less). However, it is likely that this object has a weak, broad Hα line, and its companion (which has a very reddened H II or Sey 2 spectrum) may also contribute to the X-ray flux.

4.2.2.3. Normal Star-forming Galaxies

Five of the 13 H II galaxies we observed have L_X in the range $1–4 \times 10^{42}$ ergs s^{-1}, which makes them more luminous than all other normal H II galaxies detected at X-ray wavelengths, but by less than a factor of 10 (Fabbiano 1989). These may indeed be very luminous H II galaxies, which, assuming they are rare, we are finding because we have examined a large sample of faint X-ray sources. But evidence continues to mount against the existence of *any* starburst galaxies with L_X substantially in excess of 10^{42} ergs s^{-1} (Moran et al. 1995; Halpern, Helfand, & Moran 1995), and we must approach this issue cautiously. All five high-L_X H II galaxies are low-significance detections, and there is likely to be considerable uncertainty in their X-ray fluxes. Furthermore, since $\sigma < 3.1$ for all five objects, they could *all* be the expected chance coincidences in our list. The X-ray source in one case, $16008 + 3339$, may actually be a nearby M star. On the other hand, we know that many of our low-σ X-ray sources are real. In particular, our $z = 3.87$ quasar $1745 + 6228$, discussed in § 4.1.2, is listed as a 2.59 σ source in our catalog. *ROSAT* observations have confirmed the existence of this X-ray source (Fink & Briel 1993). Similarly, the Seyfert 1.9 galaxy $14060 + 7207$, a 3.2 σ detection in this sample, was detected in the *ROSAT* All-Sky Survey (Boller et al. 1992). The X-ray identifications of these possible high-L_X H II galaxies should also be confirmed with other X-ray observations.

4.2.2.4. "Starburst/Seyfert Composite" Galaxies

With the exception of $16075 + 2838$, the most surprising result from the optical identification of these IPC/FSC sources has been the discovery of three objects whose optical spectra indicate both vigorous star formation and Seyfert activity. We tentatively call these objects starburst/Seyfert composite galaxies, or simply "composites." The emission-line flux ratios for these galaxies place them either between the areas occupied by Seyferts and H II galaxies on the standard diagnostic diagrams (e.g., Veilleux & Osterbrock 1987) or, in one case, solidly in the H II galaxy area. Furthermore, most of the emission lines are very narrow (velocity widths less than 300 km s^{-1}), also typical for H II galaxies. However, all three of the composites have [O III] line widths substantially greater (by 100–280 km s^{-1}) than those of *all* other lines in the spectrum. In addition, two of the galaxies display faint, broad wings on the Hα line. These features can only be interpreted as evidence for an active nucleus. The computed X-ray luminosities for all three composites exceed 10^{42} ergs s^{-1}, a further indication that they harbor active nuclei. Examples of their spectra are displayed in Figure 15, and their emission-line properties are listed in Table 4.

Our interpretation of these objects is that the H II and Seyfert components contribute, in varying amounts, to the optical emission lines in these galaxies, but that the Seyfert component is primarily responsible for the X-ray emission. Four similar galaxies were discussed by Véron, Véron, & Zuiderwijk (1981) and Véron et al. (1981), who came to the same conclusions regarding their composite nature. It is not clear at present whether there is any relation between the composite objects and $16075 + 2838$, which has extremely
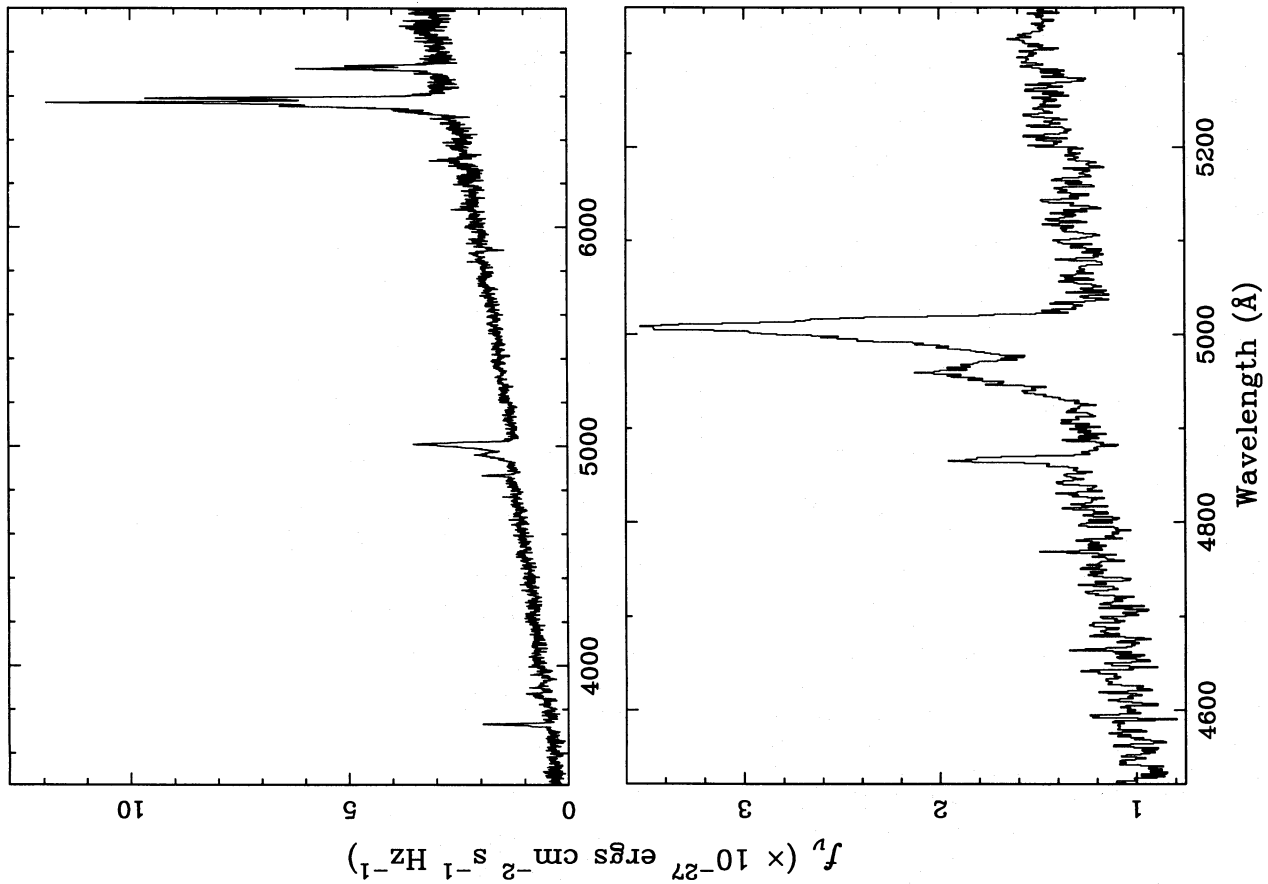
FIG. 14.—The unusual spectrum of *IRAS* F16075+2838, and detail of the [O III], Hβ region
FIG. 15.—Spectrum of *IRAS* F08255+2630 (*top*), a starburst/Seyfert composite object, has primarily starburst galaxy characteristics. However, a close look at the [O III], Hβ region (*middle*) reveals broad [O III] lines (FWHM = 377 km s⁻¹), which must arise in an AGN. The spectrum of another composite object, F01445+3503 (*bottom*) indicates a weak, broad Hα feature as well, not present in F08255+2630.
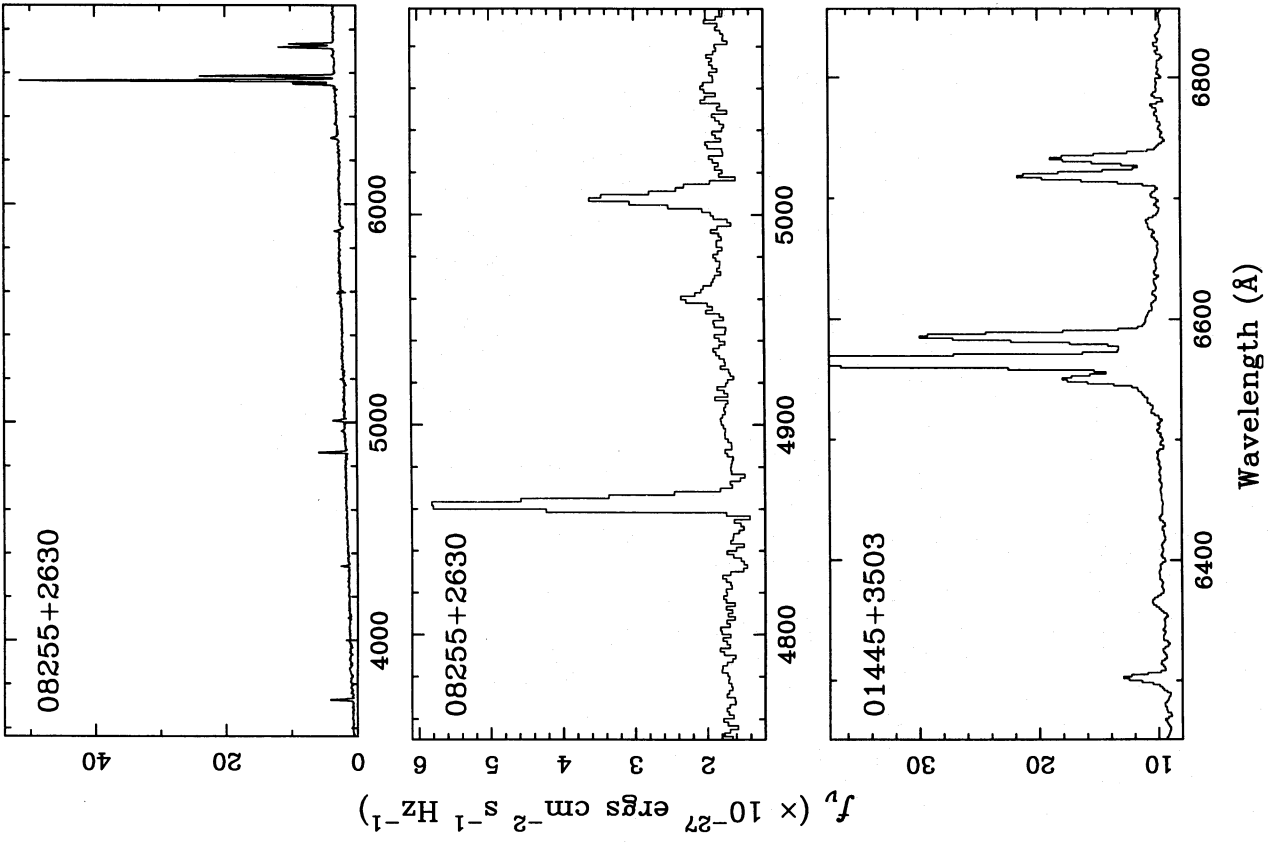
TABLE 4

STARBURST/SEYFERT COMPOSITE GALAXIES: EMISSION-LINE MEASUREMENTS

OBJECT	z	$\log L_X$[b]	[FLUX/F(Hβ)]/VELOCITY WIDTH (km s^{-1})[a]						
			[O II]	Hβ	[O III]	[O I]	Hα[c]	[N II]	[S II][d]
01445+3503......	0.0655	42.54	2.24	1.00	3.12	0.22	4.88	1.59	1.34
			...	292	394	...	...	270	270
08255+2630......	0.0526	42.34	1.28	1.00	0.49	0.18	6.00	2.67	1.92
			...	244	377	...	...	222	217
12230+0755......	0.0372	42.46	1.08	1.00	2.67	...	9.92	8.67	3.42
			...	131	414	...	...	192	226

[a] Instrumental broadening removed.
[b] L_X in units of ergs s^{-1}.
[c] Narrow component of Hα.
[d] Flux for [S II] $\lambda\lambda6716, 6731$; velocity width is for the individual components.

broad [O III] lines. Because of the optical weakness of the Seyfert component in the composites, it is likely that different mechanisms are responsible.

The mix of objects in our IPC/FSC sample provides an accurate preview of the unclassified sources we have observed (Moran et al. 1995) from the *ROSAT*/PSC sample of Boller et al. (1992), which includes several I Zw 1–type objects (20) and starburst/Seyfert composites (7), in addition to classical Seyferts and star-forming galaxies. The similarity of the results for these two different samples confirms that our selection and study of faint *Einstein* sources have been successful and useful.

The starburst/Seyfert composite class of galaxies represents a promising potential contributor to the XRB. These objects are appealing in this role because they are luminous X-ray sources but are optically discreet about their nuclear activity. They may have gone largely unnoticed in the past because very high quality optical spectra are required to reveal their subtle Seyfert characteristics. Their Seyfert components may appear weak optically because they are internally absorbed or, perhaps, totally obscured from our direct view. If so, their intrinsic X-ray luminosities are much higher than we observe them to be. Furthermore, their hard X-rays may be less attenuated than their soft X-rays, resulting in effectively hard emitted X-ray spectra. In this case, the composite galaxies could make an interesting contribution to the hard XRB. Detailed speculation about the nature of the composite objects is provided in Moran et al. (1995).

5. SUMMARY

We have presented new analysis of the *Einstein Observatory* IPC database and have assembled a catalog of sources and fluctuations in 2520 high-latitude images exceeding 2 σ significance. Comparisons (1) of our catalog with the *Einstein* EMSS and (2) of the locations of sources on the IPC with the IPC flat field have validated our procedures for extracting sources at both high and low levels of significance. We have modeled the number of real sources in the Two-Sigma Catalog based on assumptions about the number counts/flux relation for sources in our flux range, the proportionality between source count rates and their energy fluxes, and the known vignetting and background characteristics of the IPC. The results of the model indicate that 28%, or $\sim13,000$, of the entries in the catalog are real celestial X-ray sources. This is an increase of ~9100 over the number of sources found in previous analyses of the

same 2520 IPC images. Furthermore, we have established that the fraction of spurious sources in the catalog systematically increases at increasing off-axis angles on the detector. The reliability of subsamples of sources drawn from the catalog can thus be tuned by applying different limiting signal-to-noise thresholds to sources, on the basis of their off-axis angles.

We have applied filters to the Two-Sigma Catalog in the form of astronomical catalogs at other wavelengths (i.e., from radio and infrared all-sky surveys) to select samples of special classes of X-ray sources which are themselves $\sim90\%$ reliable. Our primary objective for doing so has been to search these samples for possible new components of the cosmic X-ray background. Follow-up spectroscopy of the optical counterparts of these sources has uncovered several fascinating X-ray sources in each sample, illustrating the merits of selecting X-ray sources using a variety of methods. In the radio-selected sample, we have detected high-redshift ($z \approx 4$) quasars, which are not present in the EMSS, as well as a large number of very luminous X-ray sources that, optically, appear to be normal early-type galaxies. *ASCA* and *ROSAT* observations have been carried out to examine each of these types of objects more closely. In the infrared sample, we have discovered a Seyfert galaxy, 16075+2838, whose unusual spectrum boasts [O III] forbidden emission lines more than 1000 km s^{-1} broader than the permitted lines. A few star-forming galaxies with extreme X-ray luminosities ($>10^{42}$ ergs s^{-1}) appear in the IR sample, but their identifications as X-ray sources need confirmation. We have also discovered three luminous X-ray galaxies with composite starburst/Seyfert spectra. Because of the disparity between the X-ray and optical properties of these galaxies, these composites might represent an important new component of the X-ray background.

REFERENCES

Allen, S. W., et al. 1992, MNRAS, 259, 67
Balzano, V. A. 1983, ApJ, 268, 602
Barcons, X., & Fabian, A. C. 1990, MNRAS, 243, 366
Baum, S. A., Heckman, T., Bridle, A., van Breugel, W., & Miley, G. 1988, ApJS, 68, 643
Bechtold, J., et al. 1994a, AJ, 108, 374
———. 1994b, AJ, 108, 759
Becker, R. H., Helfand, D. J., & White, R. L. 1992, AJ, 104, 531
Becker, R. H., White, R. L., & Edwards, A. L. 1991, ApJS, 75, 1
Becker, R. H., White, R. L., & Helfand, D. J. 1995, ApJ, 450, 559
Boller, T., Meurs, E. J. A., Brinkmann, W., Fink, H., Zimmermann, U., & Adorf, H.-M. 1992, A&A, 261, 57
Boyle, B. J., Staveley-Smith, L., Stewart, G. C., Georgantopoulos, I., Shanks, T., & Griffiths, R. E. 1993, MNRAS, 265, 501
Brinkmann, W., Siebert, J., & Boller, T. 1994, A&A, 281, 355
Comastri, A., Setti, G., Zamorani, G., & Hasinger, G. 1995, A&A, 296, 1
Condon, J. J., Broderick, J. J., & Seielstad, G. A. 1989, AJ, 97, 1064
David, L. P., Jones, C., & Forman, W. 1992, ApJ, 388, 82
Della Ceca, R., Zamorani, G., Maccacaro, T., Wolter, A., Griffiths, R., Stocke, J. T., & Setti, G. 1994, ApJ, 430, 533
Elvis, M., Fiore, F., Wilkes, B., McDowell, J., & Bechtold, J. 1994, ApJ, 422, 60
Elvis, M., Schreier, E. J., Tonry, J., Davis, M., & Huchra, J. P. 1981, ApJ, 246, 20
Fabbiano, G. 1989, ARA&A, 27, 87
Fabbiano, G., Gioia, I. M., & Trinchieri, G. 1989, ApJ, 347, 127
Fabbiano, G., Miller, L., Trinchieri, G., Longair, M., & Elvis, M. 1984, ApJ, 277, 115
Fabian, A. C., & Barcons, X. 1992, ARA&A, 30, 429
Filippenko, A. V., & Terlevich, R. 1992, ApJ, 397, L79
Fink, H., & Briel, U. G. 1993, A&A, 274, L45
Fruscione, A., & Griffiths, R. E. 1991, ApJ, 380, L13
Gelderman, R., & Whittle, M. 1994, ApJS, 91, 491
Giacconi, R., et al. 1979, ApJ, 234, L1
Gioia, I. M., Maccacaro, T., Schild, R. E., Stocke, J. T., Liebert, J. W., Danziger, I. J., Kunth, D., & Lub, J. 1984, ApJ, 283, 495
Gioia, I. M., Maccacaro, T., Schild, R. E., Wolter, A., Stocke, J. T., Morris, S. L., & Henry, J. P. 1990, ApJS, 72, 567
Green, P. J., Anderson, S. F., & Ward, M. J. 1992, MNRAS, 254, 30
Griffiths, R. E., et al. 1983, ApJ, 269, 375
Griffiths, R. E., & Padovani, P. 1990, ApJ, 360, 483
Halpern, J. P., Helfand, D. J., & Moran, E. C. 1995, ApJ, 453, 611
Halpern, J. P., & Oke, J. B. 1987, ApJ, 312, 91
Hamilton, T. T., & Helfand, D. J. 1987, ApJ, 318, 93
———. 1993, ApJ, 418, 55
Hamilton, T. T., Helfand, D. J., & Wu, X. 1991, ApJ, 379, 576
Harnden, F. R., Fabricant, D. G., Harris, D. E., & Schwarz, J. 1984, SAO Spec. Rep. No. 393
Harris, D. E., et al. 1990, The *Einstein Observatory* Catalog of IPC X-Ray Sources (Cambridge: SAO)
Hasinger, G., Burg, R., Giacconi, R., Hartner, G., Schmidt, M., Trümper, J., & Zamorani, G. 1993, A&A, 275, 1
Henry, J. P., et al. 1994, AJ, 107, 1270
Hook, I. M., McMahon, R. G., Patnaik, A. R., Browne, I. W. A., Wilkinson, P. N., Irwin, M. J., & Hazard, C. 1995, MNRAS, 273, L63
Kirhakos, S. D., & Steiner, J. E. 1990, AJ, 99, 1722
Kollgaard, R. I., Wardle, J. F. C., Roberts, D. H., & Gabuzda, D. C. 1992, AJ, 104, 1687
Maccacaro, T., Della Ceca, R., Gioia, I. M., Morris, S. L., Stocke, J. T., & Wolter, A. 1991, ApJ, 374, 117
Maccacaro, T., et al. 1982, ApJ, 253, 504
Madau, P., Ghisellini, G., & Fabian, A. C. 1994, MNRAS, 270, L17
Mather, J. C., et al. 1990, ApJ, 354, L37
Moran, E. C., Halpern, J. P., Bothun, G. D., & Becker, R. H. 1992, AJ, 104, 990
Moran, E. C., Halpern, J. P., & Helfand, D. J. 1994, ApJ, 433, L65
———. 1995, ApJS, submitted
Moran, E. C., Helfand, D. J., & Becker, R. H. 1996, in preparation
Morris, S. L., Stocke, J. T., Gioia, I. M., Schild, R. E., Wolter, A., Maccacaro, T., & Della Ceca, R. 1991, ApJ, 380, 49
Moshir, M., et al. 1992, Explanatory Supplement to the *IRAS* Faint Source Survey, Version 2, JPL D-10015 8/92 (Pasadena: JPL)
Oppenheimer, B. R., Gaidos, E. J., & Helfand, D. J. 1996, in preparation
Osterbrock, D. E., & Shaw, R. A. 1988, ApJ, 327, 89
Pickering, T. E., Impey, C. D., & Foltz, C. B. 1994, AJ, 108, 1542
Ponman, T. J., & Bertram, D. 1993, Nature, 363, 51
Primini, F. A., Murray, S. S., Huchra, J., Schild, R., Burg, R., & Giacconi, R. 1991, ApJ, 374, 440
Schmidt, M., van Gorkom, J. H., Schneider, D. P., & Gunn, J. E. 1995, AJ, 109, 473
Stark, A. A., Gammie, C. F., Wilson, R. W., Bally, J., Linke, R. A., Heiles, C., & Hurwitz, M. 1992, ApJS, 79, 77
Stephens, S. A. 1989, AJ, 97, 10
Stocke, J. T., Morris, S. L., Gioia, I. M., Maccacaro, T., Schild, R., Wolter, A., Fleming, T. A., & Henry, J. P. 1991, ApJS, 76, 813
Tananbaum, H., et al. 1979, ApJ, 234, L9
Ulvestad, J. S., & Wilson, A. S. 1989, ApJ, 343, 659
Veilleux, S., & Osterbrock, D. E. 1987, ApJS, 63, 295
Véron, M. P., Véron, P., & Zuiderwijk, E. J. 1981, A&A, 98, 34
Véron, P., Véron, M. P., Bergeron, J., & Zuiderwijk, E. J. 1981, A&A, 97, 71
Wang, Q., Hamilton, T. T., Helfand, D. J., & Wu, X. 1991, ApJ, 374, 475
White, R. L., & Becker, R. H. 1992, ApJS, 79, 331
Whittle, M., Pedlar, A., Meurs, E. J. A., Unger, S. W., Axon, D. J., & Ward, M. J. 1988, ApJ, 326, 125
Wilkes, B. J., Tananbaum, H., Worrall, D. M., Avni, Y., Oey, M. S., & Flanagan, J. 1994, ApJS, 92, 53
Worrall, D. M., Giommi, P., Tananbaum, H., & Zamorani, G. 1987, ApJ, 313, 596
Wu, X., Hamilton, T., Helfand, D. J., & Wang, Q. 1991, ApJ, 379, 564